Mechanoaccumulative elements of the mammalian actin cytoskeleton

Schiffhauer, Eric S.; Luo, Tianzhi; Mohan, Krithika; Srivastava, Vasudha; Qian, Xuyu; Griffis, Eric R.; Iglesias, Pablo A.; Robinson, Douglas N.

Published in:
Current Biology

DOI:
10.1016/j.cub.2016.04.007

Publication date:
2016

Document Version
Accepted author manuscript

Title: Mechanoaccumulative Elements of the Mammalian Actin Cytoskeleton

Authors: Eric S. Schiffhauer [1,#], Tianzhi Luo [1,#,†], Krithika Mohan [3], Vasudha Srivastava [4], Xuyu Qian [5], Eric R. Griffis[6], Pablo A. Iglesias [1,3,5], and Douglas N. Robinson [1,2,4*]

Affiliations

[1] Department of Cell Biology and [2] Department of Pharmacology and Molecular Science, School of Medicine, Johns Hopkins University, Baltimore, MD, 21205, USA

[3] Department of Electrical and Computer Engineering, [4] Department of Chemical and Biomolecular Engineering, and [5] Department of Biomedical Engineering, Whiting School of Engineering, Johns Hopkins University, Baltimore, MD, 21218, USA

[6]Centre for Gene Regulation and Expression, School of Life Sciences, University of Dundee, Dundee, DD1 5EH, UK

# These authors contributed equally.

* To whom correspondence should be addressed: D. N. Robinson at dnr@jhmi.edu

† Current address for Tianzhi Luo: Department of Modern Mechanics, University of Science and Technology of China

Running Title: Mechanosensitive elements of the cytoskeleton

Abstract
To change shape, divide, form junctions, and migrate, cells reorganize their cytoskeletons in response to changing mechanical environments [1-4]. Actin cytoskeletal elements, including myosin II motors and actin crosslinkers, structurally remodel and activate signaling pathways in response to imposed stresses [5-9]. Recent studies demonstrate the importance of force-dependent structural rearrangement of α-catenin in adherens junctions [10] and vinculin's molecular clutch mechanism in focal adhesions [11]. However, the complete landscape of cytoskeletal mechanoresponsive proteins and the mechanisms by which these elements sense and respond to force remain to be elucidated. To find mechanosensitive elements in mammalian cells, we examined protein relocalization in response to controlled external stresses applied to individual cells. Here, we show that non-muscle myosin II, α-actinin, and filamin accumulate to mechanically stressed regions in cells from diverse lineages. Using reaction-diffusion models for force-sensitive binding, we successfully predicted which mammalian α-actinin and filamin paralogs would be mechanoaccumulative. Furthermore, a Goldilocks zone must exist for each protein where the actin-binding affinity must be optimal for accumulation. In addition, we leveraged genetic mutants to gain a molecular understanding of the mechanisms of α-actinin and filamin catch-bonding behavior. Two distinct modes of mechanoaccumulation can be observed: a fast, diffusion-based accumulation and a slower, myosin II-dependent cortical flow phase that acts on proteins with specific binding lifetimes. Finally, we uncovered cell-type and cell-cycle-stage-specific control of the mechanosensation of myosin IIB, but not myosin IIA or IIC. Overall, these mechanoaccumulative mechanisms drive the cell's response to physical perturbation during proper tissue development and disease.

Highlights

- α-actinin, filamin and myosin II paralogs are major mechanoaccumulative proteins.
- *Dictyostelium*-developed models predict mammalian paralog-specific mechanoresponses.
- Diffusion-mediated accumulation can be separated from myosin II-driven flow.
- Cooperativity and catch bonds define a Goldilocks zone for mechanoaccumulation.

In Brief
The actin cytoskeleton controls cellular shape change during normal development and in disease processes. Schiffhauer *et al.* discover mammalian cytoskeletal proteins that accumulate in response to stress and outline molecular mechanisms driving this accumulation. These proteins comprise the cell's network-scale response to control cell shape.

Results and Discussion

To identify mechanosensitive elements, we examined protein relocalization in response to controlled external stresses applied locally to individual cells. We characterized more than 20 actin-binding, signaling, and lipid-binding proteins by transiently expressing fluorescently-tagged constructs in Jurkat T-cells (**Fig. 1**), NIH 3T3 fibroblasts (**Fig. S1A**), HeLas (**Fig. S1B**), and HEK 293Ts (**Fig. S1C**). Cells were deformed into the pipette by micropipette aspiration (MPA) [12] to a length twice the radius of the pipette ($2L_p/R_p$) for five minutes using a fixed pressure defined by their mechanical properties (Jurkat: 0.075 nN/μm^2; NIH 3T3: 0.15 nN/μm^2; HEK 293T: 0.15 nN/μm^2; HeLa: 0.2 nN/μm^2). We have previously determined computationally that the tip region in the pipette is the region of highest dilational deformation, while the pipette neck experiences shear deformation [13]. The concept of dilation of the cytoskeleton at the tip region is also supported by the immediate decrease in actin density upon deformation by MPA (not shown), similar to what has been observed in red blood cells [14]. Furthermore, although the actin network has a very fast recovery time, a significant immobile fraction exists, which is likely to be the network that experiences these two modes of deformation [15]. Maximal protein accumulation in response to dilational deformation was quantified by normalizing the fluorescence intensity of the cortex in the tip region (I_t) to that of the unstressed cortex opposite the pipette (I_o) (**Fig. 1**). The blue bar represents the 95% confidence interval for cytosolic GFP quantified in the same manner, a control used in all cell types to denote the threshold over which a protein must accumulate to be significantly mechanosensitive. The response of the majority of proteins fell within this confidence interval, implying their insensitivity towards dilational deformation in all cell types. The greatest accumulative responses were observed in actin-binding proteins, including the myosin IIs. The extent of myosin accumulation did not correlate with the radius of the pipette, ruling out accumulation due to specific local membrane curvature **(Fig S2D)**. In addition, the curvature-sensing protein i-BAR showed no accumulation (**Fig S1B**), supporting the notion that the observed accumulations are due to mechanical stress sensing rather than curvature sensing. We selected the highly accumulative myosin II, α-actinin, and filamin for further characterization.

Non-muscle myosin II is an established part of a mechanosensitive system both in *Dictyostelium* and *Drosophila*, where it accumulates at the site of applied forces and drives cellular contraction [9, 12-13, 16]. The magnitude of accumulation depends on the net force on each myosin II head and requires the presence of actin-crosslinkers to anchor actin filaments [13, 17-19]. Mammalian cells express three paralogs of non-muscle myosin II: IIA (MYH9), IIB (MYH10), and IIC (MYH14). By examining differences in accumulation of these paralogs across multiple cell lines during MPA, we aimed to uncover how the mechanoresponsiveness of this important mechanoenzyme is regulated in mammalian cells. The paralogs have differing duty ratios [19], unique force-dependent affinities to F-actin [20], and distinct spatial distributions in migrating cells [19-22], suggesting non-overlapping roles for the myosin II paralogs. Several studies revealed that cells respond to their mechanical environment by modifying or regulating the expression of these distinct myosin IIs [5, 21, 23, 24].

In response to dilational stress, we found myosin IIA and IIC exhibited a characteristic accumulation curve in all cell types, showing a short (30-70s) delay followed by a sigmoidal rise in protein intensity, plateauing by 150-200s (**Fig. 2A,C**). This biphasic behavior is characteristic of cooperative binding interactions, a behavior we previously modeled for *Dictyostelium* myosin II [25]. The network stress-dependent stalling of myosin II heads in the strongly-bound state

during the myosin power stroke gives rise to this cooperativity and promotes bipolar thick filament assembly [9, 13, 18, 26]. Once the accumulated myosin II fully opposes the applied stress, the bound heads do not experience increasing stress, resulting in maximal accumulation [13, 25].

Interestingly, while the accumulation kinetics for myosin IIA and IIC were nearly identical between cell types, myosin IIB showed highly cell-type and cell-cycle-stage specific behavior. In Jurkats, myosin IIB was the most mechanoresponsive paralog, achieving greater than two-fold normalized intensity relative to the opposite cortex. In HeLa cells, myosin IIB accumulated moderately, while in NIH 3T3 cells, no appreciable accumulation was detected (**Fig. 2B**). This difference in accumulation did not correlate with endogenous expression levels (**Fig. S2B inset**) or the cortical tensions of the cell types (**Fig. S2B**). It is unlikely that the accumulation of any paralog can be attributed to co-assembly with another, given the consistent behavior of myosin IIA and IIC in cells endogenously expressing very different quantities of all three proteins. In fact, while the mechanoresponse of myosin IIB correlated with IIA expression for these first three cell types, Cos-7 cells, which lack myosin IIA (**Fig. S2B inset**), showed robust myosin IIB accumulation (**Fig. S2C**), demonstrating that IIB's mechanoresponse is independent of IIA. In addition, the accumulation of myosin IIB exceeded that of any other myosin II in Jurkat cells and did not accumulate in 3T3s despite the presence and accumulation of myosin IIA. Further, while myosin IIA showed no change in mechanoresponse over the cell cycle in HeLa cells (**Fig. 2E, Fig. S3A,B**), the myosin IIB mechanoresponse is cell cycle phase-specific; it accumulates in interphase and metaphase but not anaphase (**Fig. 2F, Fig. S3A,B**). This cell-cycle specificity implicates relatively transient regulatory mechanisms for the myosin IIB mechanoresponse that tune cellular shape-change during cytokinesis. One explanation is the phosphoregulation of IIB is distinct from that of IIA and IIC. Indeed, a short serine-rich stretch within the assembly domain of IIB confers its distinct localization pattern and behavior in cells in a phosphorylation-dependent manner [27], and this regulation could also affect myosin IIB mechanoaccumulation.

Force sharing among actin crosslinkers is also important for cellular mechanoresponsiveness [13]. From our search for mechanoresponsive elements, the actin crosslinkers α-actinin 4 and filamin B strongly responded. Interestingly, α-actinin 1 and filamin A did not accumulate significantly in any cell type. Thus, we examined what factors could lead to such paralog-specific differences. We previously characterized the force-dependent accumulation of the *Dictyostelium* α-actinin and filamin to dilated and sheared regions, respectively [13]. In the absence of myosin II, we determined α-actinin strongly accumulated to dilated regions of the cell with significantly faster kinetics than myosin II. In contrast, filamin displayed rapid, cooperative, local enrichment in sheared regions at the pipette neck [13].

We modified a reaction-diffusion model first developed for *Dictyostelium* α-actinin [13] to predict mammalian α-actinin accumulative behavior (**Fig. 3A**), by using measured binding affinities for mammalian α-actinin 1 (K_d= 0.36 μM) or α-actinin 4 (K_d= 32 μM) without altering the other parameters (**Table S1**). This model assumes the binding lifetime of α-actinin increases upon the application of force due to catch-bond behavior. Simulations of the model predicted that, owing to intrinsic differences in their initial binding affinities, α-actinin 4, but not α-actinin 1, would accumulate in response to deformation (**Fig. 3A**). During MPA, α-actinin 4 strongly accumulated in Jurkat cells with a curve shape strikingly similar to those in the simulations, while α-actinin 1 did not accumulate (**Fig. 3B**). However, the experimentally observed accumulation of α-actinin 4 was about 25 times slower than in the simulations. This difference is

partly explained by a slower α-actinin rate of diffusion (3.7±0.2 $\mu m^2/s$ as measured by Fluorescence Correlation Spectroscopy (FCS) in **Figure S4D-F**, compared to 10 $\mu m^2/s$ used in the original model) and longer actin filaments in the mammalian cytoskeleton compared with *Dictyostelium* [28]. To fully recapitulate the experiment, the on and off rates of actin-binding had to be slowed eight-fold, suggesting a level of mammalian α-actinin regulation not seen in *Dictyostelium* (**Fig. S4A**). Here, through the use of modeling, we showed the initial binding affinity of an actin crosslinker dictates its general mechanoaccumulative behavior. In the model, the rapid accumulation of the lower-affinity α-actinin 4 is driven by a high rate of exchange with the actin network and a large pool of the unbound species. This dynamic crosslinker exchange can explain the rapid and dramatic changes in localization as the crosslinkers lock onto the network in response to mechanical stress. Further, actin-binding affinity must be low enough for there to be an available pool of cross-linkers for mechanoaccumulation to occur, but high enough for the protein to bind; hence a Goldilocks zone of affinity is suggested – not too high, not too low, just right.

To probe the molecular mechanism of α-actinin catch-bond behavior, we analyzed the α-actinin actin-binding domain (ABD), which is highly conserved among actin binding proteins [29]. This domain consists of two calponin homology (CH) domains, each with an actin-binding site, that are normally tethered in a closed conformation by a salt bridge at the CH-CH interface. A mutation of lysine-255 to glutamate (K255E) in α-actinin 4 disrupts this salt bridge, driving the molecule into a permanently open configuration and revealing a third actin-binding site. *In vitro*, the K255E mutant has a five-fold higher actin binding affinity than the wild-type protein [30, 31]. We hypothesized that network stress disrupts the salt bridge and converts the protein into the open, high affinity conformation, giving rise to catch-bond behavior of WT α-actinin 4 and leading to localized, stress-dependent accumulation. To test this, we analyzed the mechanoaccumulation kinetics of the K255E mutant, which we hypothesized lacks this mechanosensitive switch. Indeed, α-actinin 4 K255E did not accumulate in the first 100 s of aspiration. However, the mutant began to accumulate after 100 s (**Fig 3C**) with accumulation kinetics mirroring those of myosin II (**Fig. 2**). Therefore, we tested the role of myosin II by inhibiting the mechanoresponse of the three myosins with the myosin light chain kinase inhibitor ML7 (**Fig. S2E**). Upon the addition of 30 μM ML7, wild-type α-actinin 4 protein still accumulated considerably, while the K255E mutant did not (**Fig. 2D**). To rule out off-target effects of ML7, we independently verified the result using 10 μM Y-27632, an inhibitor of the Rho-associated kinase ROCK, which also regulates myosin light chain phosphorylation. The results were nearly identical for the two inhibitors **(Fig. S2E).** The model predicts that a simple five-fold change in actin-binding affinity would not prevent α-actinin 4 accumulation (**Fig. S4B**), suggesting the K255E mutation perturbs α-actinin's mechanism of mechanoresponse.

To assess the necessity of the salt bridge for catch-bonding, we analyzed the fluorescence recovery after photobleaching (FRAP) of both wild-type and mutant α-actinin 4 in HeLa cells in the absence or presence of compressive stress (**Fig. 3E**). Cells were compressed with a thin sheet of agarose, reducing their height by a roughly a factor of 2. We have demonstrated previously that this technique drives the accumulation of mechanosensitive proteins, including myosin II and cortexillin, to the cell's lateral edges where dilation is highest [13] as the cell actively resists the applied load [15]. Although the exact force felt by the cytoskeleton is difficult to quantify in this technique, the recovery time (τ) of proteins that lock onto the cytoskeleton under physiologically-relevant applied loads increases [15]. The K255E mutant localized to stress fibers more readily than the wild-type even without applied stress, but all FRAP measurements

were taken from the cell cortex (**Fig. 3E**). Similar to a previous report [31], the higher affinity K255E mutant showed much slower recovery than wild-type (**Fig 3F,G**). Interestingly, while wild-type α-actinin 4 showed slower recovery under agarose overlay, the K255E mutant showed no significant change in recovery time (τ) or immobile fraction (**Fig. 3F,G, Fig. S4H**). Thus, the catch-bond behavior of α-actinin 4 is most likely dependent on the conversion of the highly conserved ABD from a closed to an open conformation, a change regulated by the salt bridge. In addition, a late, myosin-dependent cortical flow phase is responsible for moving the higher affinity K255E mutant to the tip region, a phenomenon we also observed with filamin (see below).

In mammalian cells, non-muscle filamins A and B form Y-shaped dimers which orthogonally crosslink actin filaments [32]. We previously found that *Dictyostelium* filamin, which forms a similar V-shaped dimer, is sensitive to shear deformation. This sensitivity manifests as an accumulation to the neck of the cell being deformed [13]. The reaction-diffusion model for filamin included cooperativity, and predicted robust accumulation of the higher affinity filamin B (K_d= 7 μM), and reduced accumulation of lower-affinity filamin A (K_d= 17 μM) (**Fig. 4A**). This is in contrast with the stronger accumulation for lower affinity α-actinin 4. While both α-actinin (non-cooperative) and filamin (cooperative) models unveil a Goldilocks zone for which the K_d is optimal for accumulation, the K_d that allows the most robust accumulation for each protein depends on whether cooperativity is present (**Fig. S4B,C**).

We were initially surprised to find that mammalian filamin B accumulated at the tip of the cell in our studies in Jurkats, instead of the neck region. Upon closer analysis, we noted that within 15 s of the pressure application, filamin B accumulated to the aspirated cell neck (**Fig. 4B**). The kinetics of this accumulation showed acceleration (**Fig. 4B**), suggesting cooperativity exists between neighboring actin-bound filamin B molecules. Longer-term tracking revealed that filamin B flows from the neck to the tip of the cell along the cortex (**Fig. 4C,E**), a process not observed in *Dictyostelium*. Filamin A failed to respond to applied pressure (**Fig. 4B,C**). Since the time scale for the tip accumulation of filamin B is ~80 s (**Fig. 4E**), along myosin II's time scale, we hypothesized that filamin B accumulation in the tip was driven by myosin II accumulation. Upon the addition of 30 μM ML7 or 10 μM Y-27632 **(Fig. S2E)**, filamin B showed normal neck accumulation (**Fig. 4D**) but did not accumulate to the tip (**Fig. 4E**). It has been shown that a filamin A mutant lacking the hinge 1 region fails to cause strain stiffening induced by its wild-type counterpart [33]. However, in our experiments, the filamin B hinge mutant showed wild-type mechanoaccumulation to either the neck or the tip of the cell (**Fig. S4I**), indicating shear-force sensation does not depend on this hinge. Thus, filamin B shows both rapid, intrinsic, shear deformation-sensitive accumulation at the cell neck, as well as myosin II-dependent cortical flow to the tip of the cell upon applied force. This myosin-dependent cortical flow resembles that seen in the α-actinin 4 K255E mutant; these two proteins have similar affinities for actin (K_d≈7 μM), which may allude to the requirement of a specific actin-binding affinity in order to be acted upon by the myosin-dependent flow. In HeLa cells, the important cytokinesis-regulator anillin also responds to the tip of the pipette, but does so exclusively during anaphase in a myosin-dependent manner (**Fig. S3D-F**). This implies a biological role for myosin-dependent accumulation in mammalian cytokinesis. These myosin-driven cortical network flows are similar to those essential for proper asymmetric cell division during *C. elegans* development [34].

In this study, we uncovered mammalian mechanosensors that accumulate under mechanical stress. We identified a Goldilocks zone of actin-binding affinities, determined by their

cooperative or non-cooperative binding properties, which dictates the maximal accumulation of these elements. We discovered two distinct modes of force-dependent accumulation: a rapid, diffusion-based mode dependent on molecular catch-bonding behavior, and a slower, myosin II-dependent cortical flow which drives actin-binding proteins to the cell tip. We also discovered the cell-type- and cell-cycle-specific mechanosensitivity of myosin IIB, which is intriguing in light of studies implicating myosin IIB as a driver of breast-cancer metastasis [35]. As growing evidence demonstrates that cell behavior is modulated by the mechanical properties of the actin network, the molecular mechanisms of the mechanoresponsive cytoskeletal elements involved become critical to understand. For example, mechanotransducing stress fibers, which dynamically form and dissolve during cell migration, are crosslinked largely by α-actinins and therefore could become more stable via α-actinin catch-bonding under load [36, 37]. In addition to genetic diseases related to filamin B and α-actinin 4 mutations [38, 39], increased expression of the mechanosensitive paralogs of α-actinin and filamin are strong negative prognosticators in multiple metastatic cancers [40-42]. Defining the mechanisms by which individual proteins and the network as a whole respond to force and determining which cytoskeletal elements are mechanosensitive is essential for elucidating normal mechanosensitive biological processes and identifying new targets for inhibiting aberrant processes in disease states.

Experimental Procedures

Experimental procedures include cell culture and transfection, live-cell fluorescence imaging, micropipette aspiration, fluorescence recovery after photobleaching, fluorescence correlation spectroscopy, drug treatments, and computational modeling. Tables of model parameters are provided in Tables S1 and S2. All statistical analysis was performed using KaleidaGraph (Synergy Software, Reading, PA). Significance of difference was determined using Analysis of Variance (ANOVA) with a Fisher's LSD post-test. The full details of methodology and materials may be found in the Supplemental Information.

Supplementary Information

Supplemental Information includes Supplemental Materials and Procedures, Tables S1 and S2, Figures S1-S4, and Supplemental References.

Author Contributions

E.S.S., T.L., E.G., V.S., and D.N.R. conceived experiments. E.S.S., T.L., V.S. and X.Q. performed experiments. K.M. and P.A.I. developed the model and carried out the simulations. E.S.S. and T.L. wrote the manuscript, V.S., K.M., E.G., P.A.I., and D.N.R. edited the manuscript.

Acknowledgments

This work is supported by the National Institutes of Health grants GM66817 and GM109863 to D.N.R., GM086704 to P.A.I. and D.N.R., and a Wellcome Trust RCDF award (090064/Z/09/Z) to E.R.G. The authors thank Mingjie Wang, Miho Iijima, Takanari Inoue, Joy Yang, Susan Craig, Allan Wells, Fumihiko Nakamura, Arnoud Sonnenberg, William Trimble, Anthony Hyman, and Michael Glotzer for their generosity with reagents. We also thank Huaqing Cai, Allen Chen and Raihan Kabir for technical assistance.

References

1. Geiger, B., Spatz, J.P., and Bershadsky, A.D. (2009). Environmental sensing through focal adhesions. Nat. Rev. Mol. Cell. Biol. *10*, 21-33.
2. Johnson, C.P., Tang, H.Y., Carag, C., Speicher, D.W., and Discher, D.E. (2007). Forced unfolding of proteins within cells. Science. *317*, 663-666.
3. DuFort, C.C., Paszek, M.J., and Weaver, V.M. (2011). Balancing forces: architectural control of mechanotransduction. Nat. Rev. Mol. Cell. Biol. *12*, 308-319.
4. Engler, A.J., Sen, S., Sweeney, H.L., and Discher, D.E. (2006). Matrix elasticity directs stem cell lineage specification. Cell. *126*, 677-689.
5. Raab, M., Swift, J., Dingal, P.C., Shah, P., Shin, J.W., and Discher, D.E. (2012). Crawling from soft to stiff matrix polarizes the cytoskeleton and phosphoregulates myosin-II heavy chain. J. Cell Biol. *199*, 669-683.
6. Chowdhury, F., Na, S., Li, D., Poh, Y.C., Tanaka, T.S., Wang, F., and Wang, N. (2010). Material properties of the cell dictate stress-induced spreading and differentiation in embryonic stem cells. Nat. Mater. *9*, 82-88.
7. Ehrlicher, A.J., Nakamura, F., Hartwig, J.H., Weitz, D.A., and Stossel, T.P. (2011). Mechanical strain in actin networks regulates FilGAP and integrin binding to filamin A. Nature *478*, 260-263.
8. Effler, J.C., Kee, Y.S., Berk, J.M., Iglesias, P.A., and Robinson, D.N. (2006). Mitosis-specific mechanosensing and contractile protein redistribution control cell shape. Curr. Biol. *16*, 1962-1967.
9. Kee, Y.S., Ren, Y., Dorfman, D., Iijima, M., Firtel, R.A., Iglesias, P.A., and Robinson, D.N. (2012). A mechanosensory system governs myosin II accumulation in dividing cells. Mol. Biol. Cell. *23*, 1510-1523.
10. Buckley, C.D., Tan, J., Anderson, K.L., Hanein, D., Volkmann, N., Weis, W.I., Nelson, W.J., and Dunn, A.R. (2014). The minimal cadherin-catenin complex binds to actin filaments under force. Science. *346*, 6209.
11. Thievessen, I. *et al.* (2013). Vinculin–actin interaction couples actin retrograde flow to focal adhesions, but is dispensable for focal adhesion growth. J. Cell Biol. *202*, 163–177
12. Kee, Y.S., and Robinson, D.N. (2013). Micropipette aspiration for studying cellular mechanosensory responses and mechanics. Methods Mol. Biol. *983*, 367-382.
13. Luo, T., Mohan, K., Iglesias, P.A., and Robinson, D.N. (2013). Molecular mechanisms of cellular mechanosensing. *Nat. Mater.* **12,** 1064-1071.
14. Discher, D., Winardi, R., Schischmanoff, P.O., Parra, M., Conboy, J.G., and Mohandas, N. (1995). Mechanochemistry of protein 4.1's spectrin-actin-binding domain: Ternary complex interactions, membrane binding, network integration, structural strengthening. J. Cell Biol. *130*, 897-907.
15. Srivastava, V. and Robinson, D.N. (2015). Mechanical stress and network structure drive protein dynamics during cytokinesis. Curr. Biol. *25*, 663-670.
16. J.H. Kim *et al.* (2015). Mechanical tension drives cell membrane fusion. Dev. Cell. *32*, 561-573.
17. Luo, T., Mohan, K., Srivastava, V., Ren, Y., Iglesias, P.A., and Robinson, D.N. (2012). Understanding the cooperative interaction between myosin II and actin crosslinkers mediated by actin filaments during mechanosensation. Biophys. J. *102*, 238-247.

18. Ren, Y., Effler, J.C., Norstrom, M., Luo, T., Firtel, R.A., Iglesias, P.A., Rock, R.S., and Robinson, D.N. (2009). Mechanosensing through cooperative interactions between myosin II and the actin crosslinker cortexillin I. Curr. Biol. *19*, 1421-1428.
19. Vicente-Manzanares, M., Ma, X., Adelstein, R.S., and Horwitz, A.R. (2009). Non-muscle myosin II takes centre stage in cell adhesion and migration. Nat Rev. Mol Cell Biol. *10,* 778–790.
20. Kovács, M., Thirumurugan, K., Knight, P.J, and Sellers, J.R. (2007). Load-dependent mechanism of nonmuscle myosin II. Proc. Natl. Acad. Sci. U.S.A. *104*, 9994-9999.
21. Shin, J.W. *et al.* (2012). Contractile forces sustain and polarize hematopoiesis from stem and progenitor cells. Cell Stem Cell. *14*, 81-93.
22. Even-Ram, S., Doyle, A.D., Conti, M.A., Matsumoto, K., Adelstein, R.S., and Yamada, K.M. (2007). Myosin IIA regulates cell motility and actomyosin-microtubule crosstalk. Nat. Cell Biol. *9*, 299-309.
23. Vicente-Manzanares, M, Koach, M.A., Whitmore, L., Lamers, M.L., and Horwitz, A.F. (2008). Segregation and activation of myosin IIB creates a rear in migrating cells. J. Cell Biol. *183*, 543-554.
24. Swift, J. *et al.* (2013). Nuclear lamin-A scales with tissue stiffness and enhances matrix-directed differentiation. Science. *341*, 1240104.
25. Mohan, K., Luo, T., Robinson, D.N., and Iglesias, P.A. (2015). Cell shape regulation through mechanosensory feedback control. J. R. Soc. Interface. *12*, DOI: 10.1098/rsif.2015.0512.
26. Orlova, A. and Egelman, E.H. (1997). Cooperative rigor binding of myosin to actin is a function of F-actin structure. J. Mol. Biol. *265*, 469-474.
27. Juanes-Garcia, A., Chapman, J.R., Aguilar-Cuenca, R., Delgado-Arevalo, C., Hodges, J., Whitmore, L.A., Shabanowitz, J., Hunt, D.F., Horwitz, A.R., and Vicente-Manzanares. (2015). A regulatory motif in nonmuscle myosin II-B regulates its role in migratory front-back polarity. J Cell Biol. *209*, 23-32.
28. Roland, J., Berro, J., Michelot, A., Blanchoin, A., and Martiel, J.L. (2008). Stochastic severing of actin filaments by actin depolymerizing factor/cofilin controls the emergence of a steady dynamical regime. Biophys. J. *6*, 2082-2094.
29. Sutherland-Smith, A.J., Moores, C.A., Norwood, F.L., Hatch, V., Craig, R., Kendrick-Jones, J., and Lehman, W. (2015). An atomic model for actin binding by the CH domains and spectrin-repeat modules of utrophin and dystrophin. J. Mol. Biol. *329*, 15–33.
30. Weins, A., Schlondorff, J.S., Nakamura, F., Denker, B.M., Hartwig, J.H., Stossel, T.P., and Pollak, M.R. (2007). Disease-associated mutant α-actinin-4 reveals a mechanism for regulating its F-actin-binding affinity. Proc. Natl. Acad. Sci. U.S.A. *104*.
31. Ehrlicher, A.J., Krishnan, R., Guo, M., Bidan, C.M., Weitz, D.A., and Pollak, M.R. (2015). Alpha-actinin binding kinetics modulate cellular dynamics and force generation. Proc. Natl. Acad. Sci. U.S.A. *112*, 6619-6624.
32. Stossel, T.P., Condeelis, J., Cooley, L., Hartwig, J.H., Noegel, A., Schleicher, M., and Shapiro, S.S. (2001). Filamins as integrators of cell mechanics and signalling. Nat. Rev. Mol. Cell Biol. *2*, 138-145.
33. Shin, J.H., Gardel, M.L., Mahadevan, L., Matsudaira, P., and Weitz, D.A. (2004). Relating microstructure to rheology of a bundled and cross-linked F-actin network in vitro. Proc. Natl. Acad. Sci. U.S.A. *101*, 9636-9641.
34. Hird, S.N. and White, J.G. (1993). Cortical and cytoplasmic flow polarity in early embryonic cells of Caenorhabditis elegans. J. Cell Biol. *121*, 1343–55.

35. Beach, J.R. *et al.* (2011). Myosin II isoform switching mediates invasiveness after TGF-β–induced epithelial–mesenchymal transition. Proc. Natl. Acad. Sci. U.S.A. *108*, 17991–17996.
36. Hotulainen, P. and Lappalainen, P. (2006). Stress fibers are generated by two distinct actin assembly mechanisms in motile cells. J. Cell Biol. *173*, 383-394.
37. Burridge, K and Wittchen, E.S. (2013). The tension mounts: Stress fibers as force-generating mechanotransducers. J. Cell Biol. *200*, 9-19.
38. Kaplan, J.M. *et al.* (2000). Mutations in ACTN4, encoding α-actinin-4, cause familial focal segmental glomerulosclerosis. Nat. Genet. *24*, 251-256.
39. Feng, Y. and Walsh, C.A. (2004). The many faces of filamin: A versatile molecular scaffold for cell motility and signalling. Nat. Cell Biol. *6*, 1034-1038.
40. Kikuchi, S. *et al.* (2008). Expression and gene amplification of actinin-4 in invasive ductal carcinoma of the pancreas. Clin. Cancer Res. *14*, 5348-5356.
41. Shao, H., Li, S., Watkins, S.C., and Wells, A. (2014). α-Actinin-4 is required for amoeboid-type invasiveness of melanoma cells. J. Biol. Chem. *289*, 32717-32728.
42. Iguchi, Y., Ishihara, S., Uchida, Y., Tajima, K., Mizutani, T., Kawabata, K., and Haga, H. (2015). Filamin B enhances the invasiveness of cancer cells into 3D collagen matrices. Cell Struct. Funct. 40, 61-67.

Figure Legends

Fig. 1. Five actin-binding proteins respond to an externally applied mechanical stress. A ratio (I_t/I_o) of maximum tip intensity (I_t) to opposite cortex intensity (I_o) shows that actin-binding proteins α-actinin 4, filamin B, myosin IIA, myosin IIB, and myosin IIC accumulated to the highest level among 22 cytoskeletal, signaling, and lipid-binding proteins in Jurkat cells (*p<0.05, **p<0.0001). Similar results are seen in 3T3, HeLa, and HEK 293T cells (**Fig. S1**)

Fig. 2. Myosin IIA and IIC show mechanoaccumulation in all contexts examined, whereas myosin IIB shows mechanoaccumulation in distinct cell types and phases of the cell cycle. (**A**) Traces of myosin IIA and (**C**) myosin IIC accumulation over time (Normalized Intensity, I_t/I_o normalized to time zero) show initial sigmoidal kinetics indicative of cooperativity, followed by a late plateau, a curve which is similar in three distinct cell types: NIH 3T3 fibroblasts, Jurkat T-cells, and HeLas (n>10 cells/trace). (**B**) Myosin IIB shows distinct kinetics and levels of mechanoresponsive plateau in the three cell types (n>10 cells/trace). (**D**) Representative images of the maximum accumulation of GFP-labeled myosins shows a similar ratio of tip intensity to opposite cortex intensity for myosin IIA and IIC in all three cells, but a very different ratio for myosin IIB (scale bar = 10 μm). (**E**) Myosin IIA behaves similarly between the phases of the cell cycle induced by treatment with STLC (metaphase) STLC+Purvalanol (anaphase) or DMSO (interphase), while (**F**) myosin IIB becomes non-mechanoresponsive in anaphase (n>9 cells/trace). Differential myosin IIB accumulation can not be explained by endogenous IIB expression, cortical tension, the mechanoresponse of myosin IIA, or differences in curvature (**Fig. S2**).

Fig 3. A force-dependent model based on actin binding affinity predicts the mechanoaccumulative behavior of α-actinins, and the high affinity α-actinin 4 mutant K255E is non-mechanoresponsive. (**A**) A reaction-diffusion catch-bond model of mechanoaccumulation derived from parameters outlined in *Dictyostelium* predicts high accumulation of mammalian α-actinin 4 and low accumulation of α-actinin 1 based on published actin-binding affinities. (**B**) This prediction captured both the protein behavior and shape of the curve in aspiration experiments in Jurkat cells (I_t/I_o normalized to time zero, n=12 cells/trace). (**C**) The α-actinin 4 K255E mutant has a five-fold higher binding affinity and shows delayed, myosin-dependent (**D**) accumulation as determined by using the pan-myosin II inhibitor ML-7 at 30 μM (n>16 cells/trace). Myosin accumulation was fully inhibited by ML-7 (**Fig. S2E**). (**E**) FRAP analysis of HeLa cells expressing GFP-α-actinin 4 and the K255E mutant in normal and compressed state. White boxes show bleached region at the time of bleaching, "Time τ" shows the level of fluorescence for each condition after one e-fold time of recovery as outlined in (**G**) (scale bar=10 μm). (**F,G**) Representative FRAP traces show a much faster recovery time for α-actinin 4 than K255E. The applied stress from agarose overlay drives slower recovery of α-actinin 4, but no change in K255E recovery (*p=0.001, **p<0.0001). Analysis of the immobile fractions are presented in **Fig. S4H**. α-actinin and filamin accumulation modeling at multiple affinities, measurement of the diffusion times used in the models, and images of compressed cells can be found in **Fig. S4**.

Figure 4. A force-dependent model based on actin binding affinity predicts the mechanoaccumulative behavior of filamins to a region of shear deformation, followed by

myosin driven cell tip accumulation. (**A**) A cooperative reaction-diffusion catch-bond model of mechanoaccumulation predicts low accumulation of filamin A and high accumulation of filamin B to the neck region of the cell, where shear deformation is highest. (**B**) In Jurkat cells, filamin A does not accumulate appreciably while filamin B accumulates to the cell neck, though initial accumulation was followed by a decay phase (I_n/I_o normalized to time zero, n=10). (**C**) This decay phase resulted from flow of filamin B, but not filamin A, from the cell neck to the cell tip (scale bars = 10 μm). (**D**) Accumulation to the cell neck was not myosin dependent (n=10). (**E**) However, flow to the cell tip was myosin II dependent. Cells in **D** and **E** were treated with DMSO or the pan-myosin II inhibitor ML-7 at 30 μM (n=12). Myosin inhibition by ML-7 is demonstrated in **Fig. S2E**.

Figure 1

Click here to download Figure SchiffhauerFigure1.tif

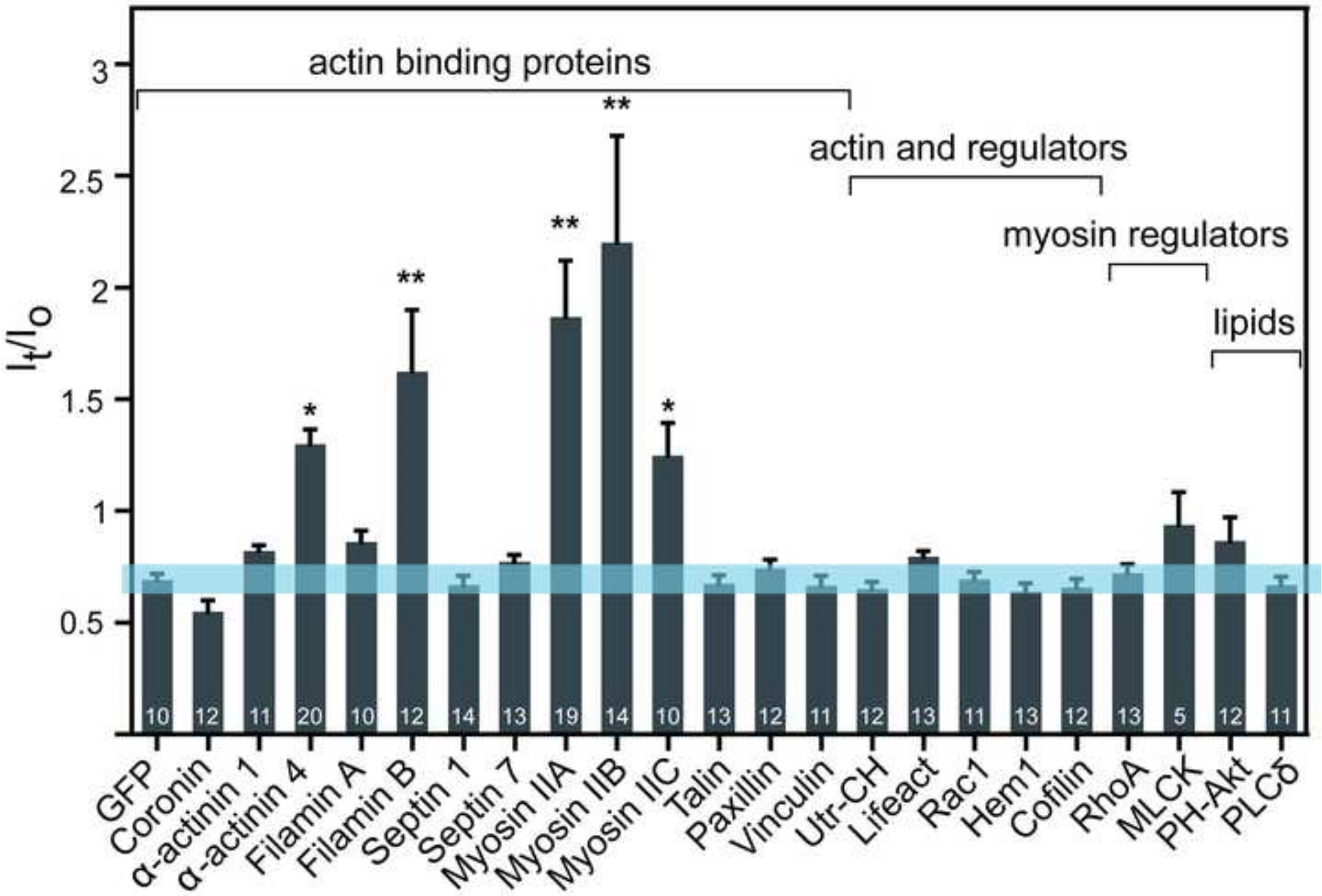

Figure 2

Click here to download Figure SchiffhauerFigure2.tif

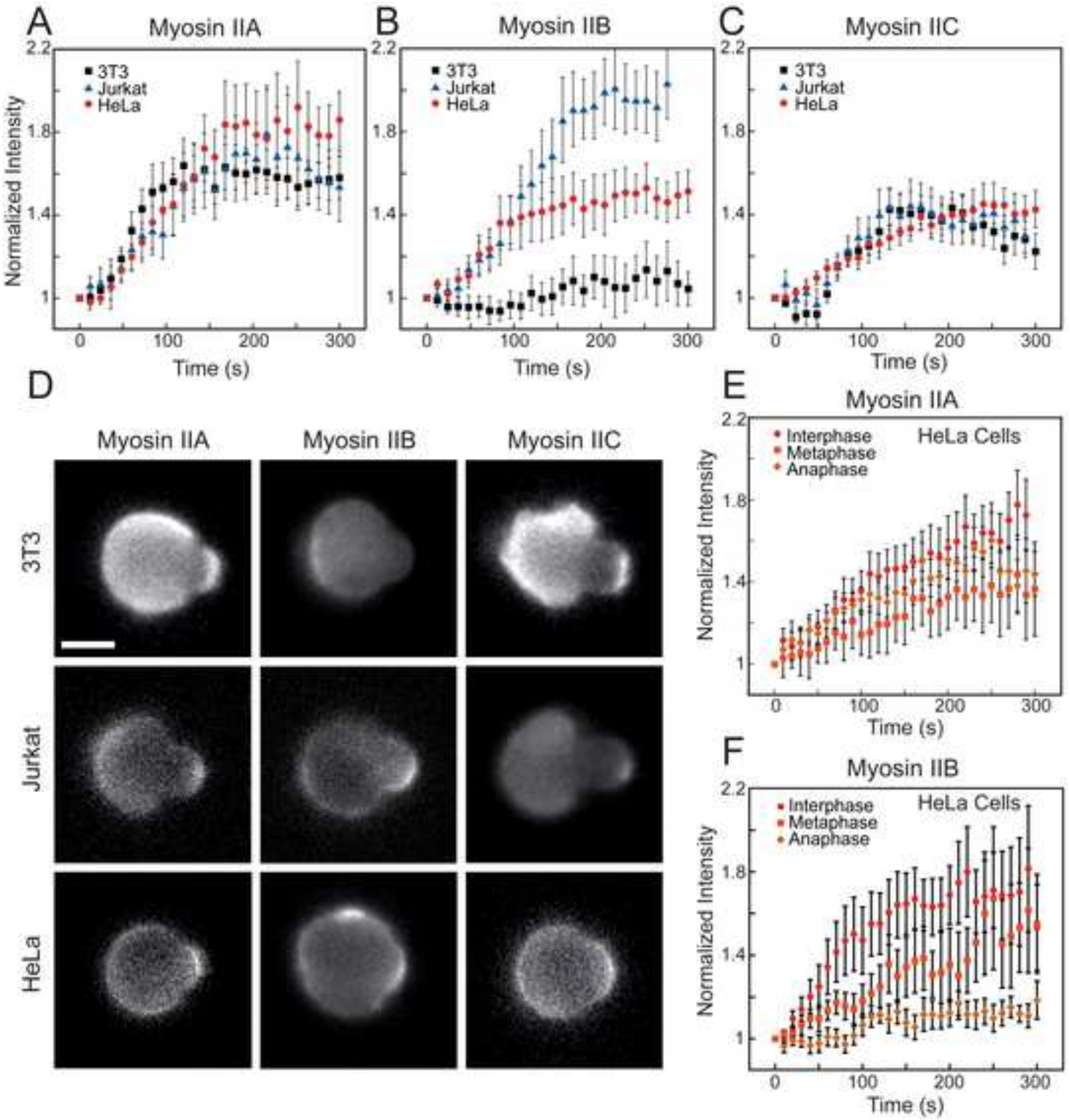

Figure 3

Click here to download Figure SchiffhauerFigure3.tif

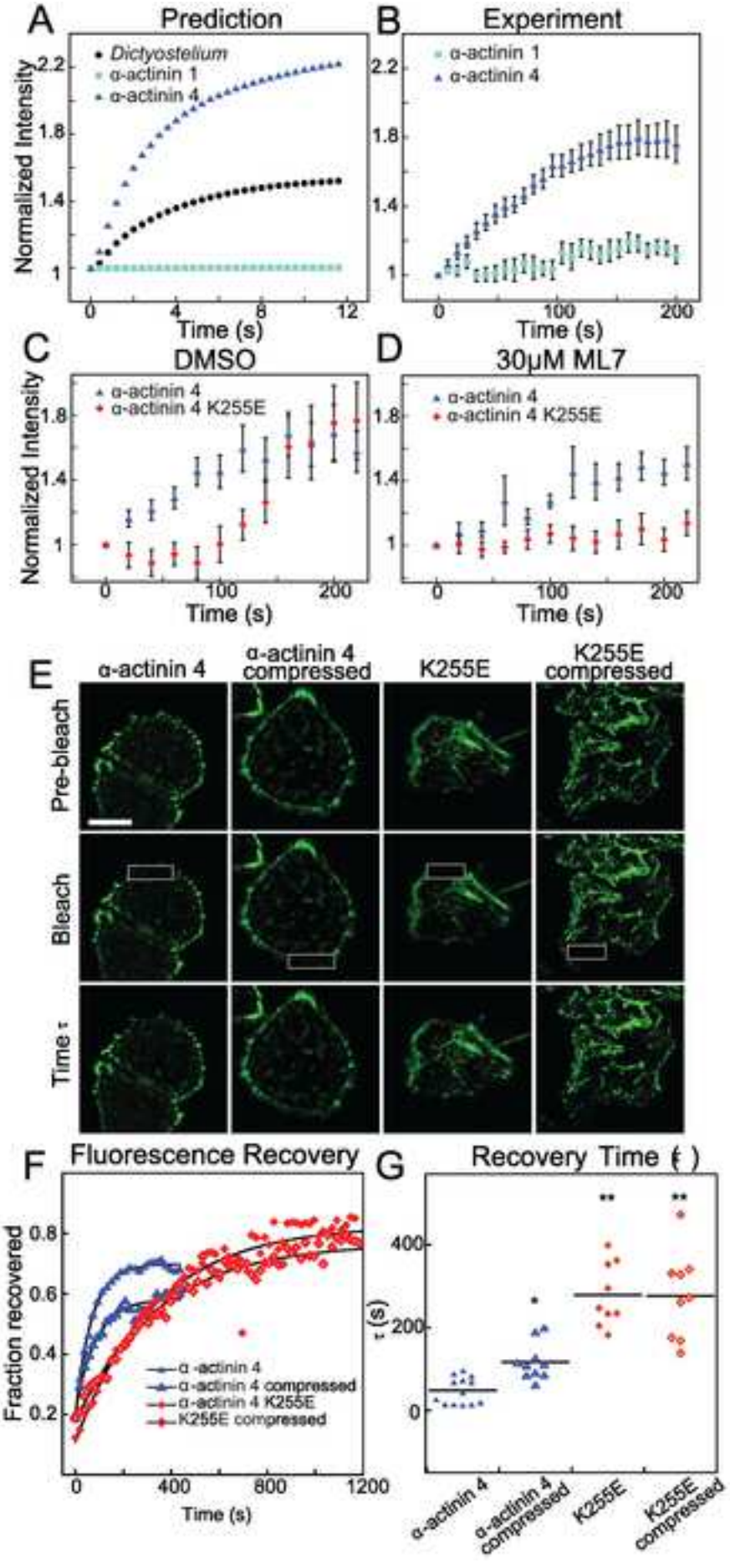

Figure 4

Click here to download Figure SchiffhauerFigure4.tif

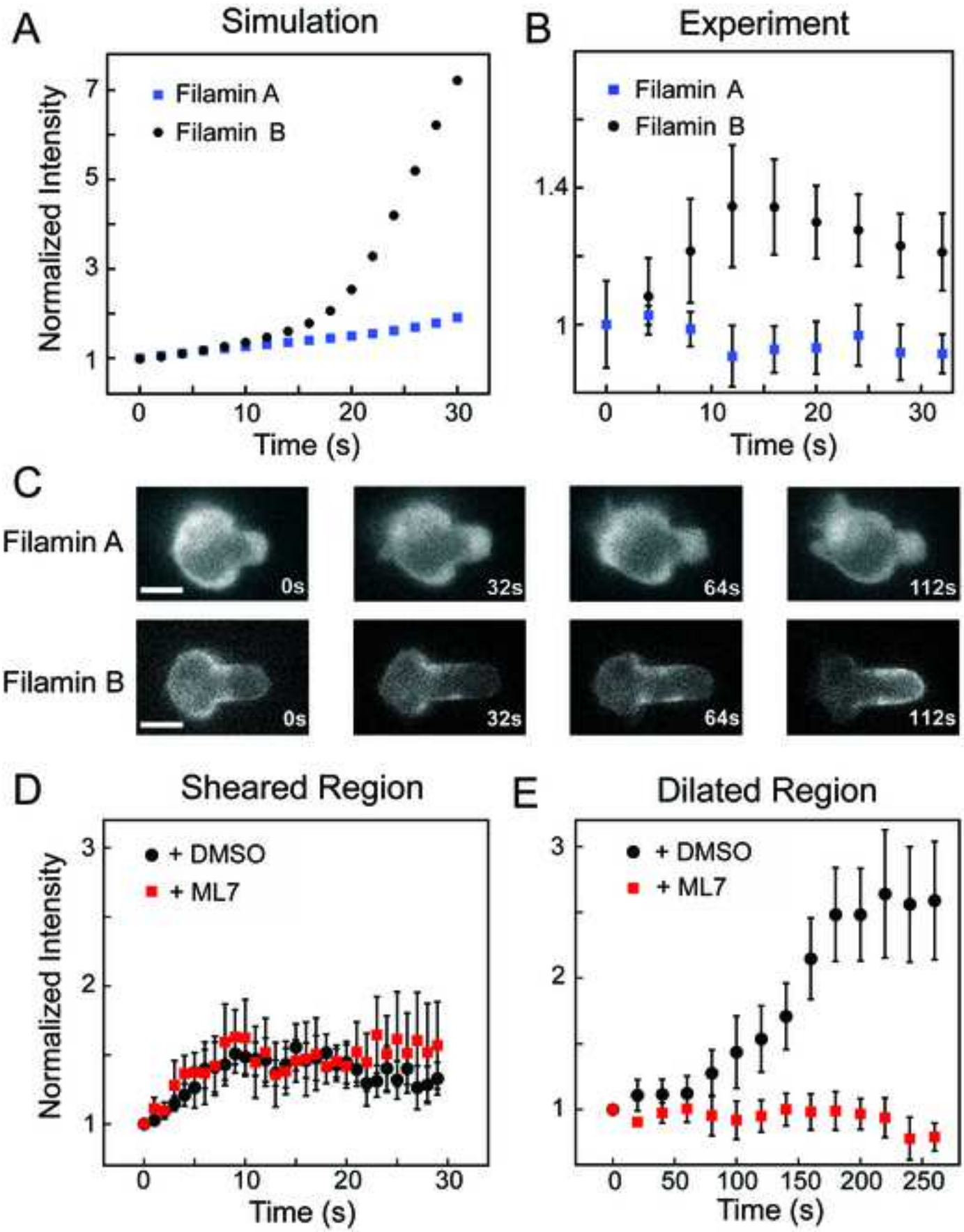

Figure S1

Click here to download Figure SchiffhauerS1.tif

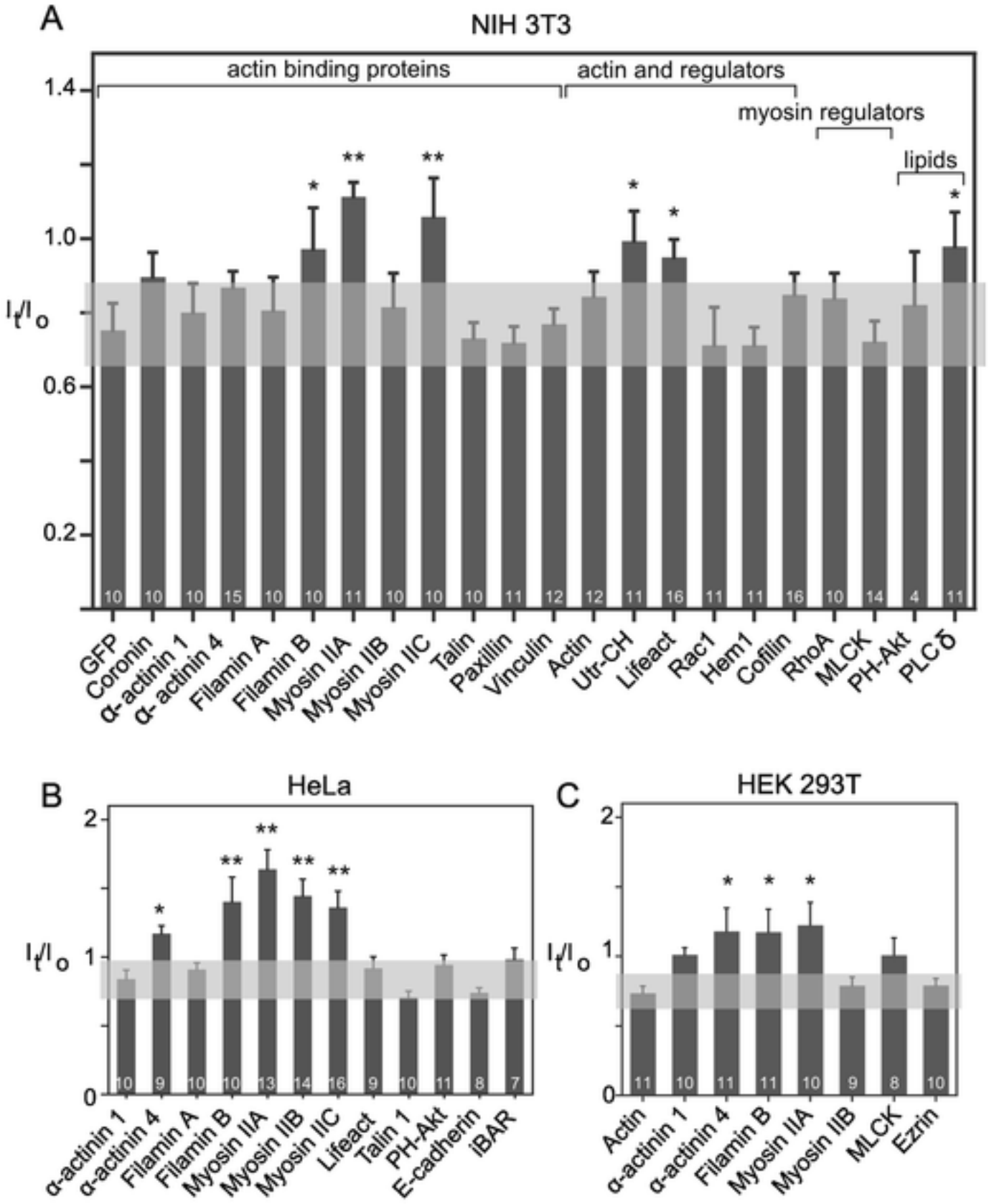

Figure S2

Click here to download Figure SchiffhauerS2.tif

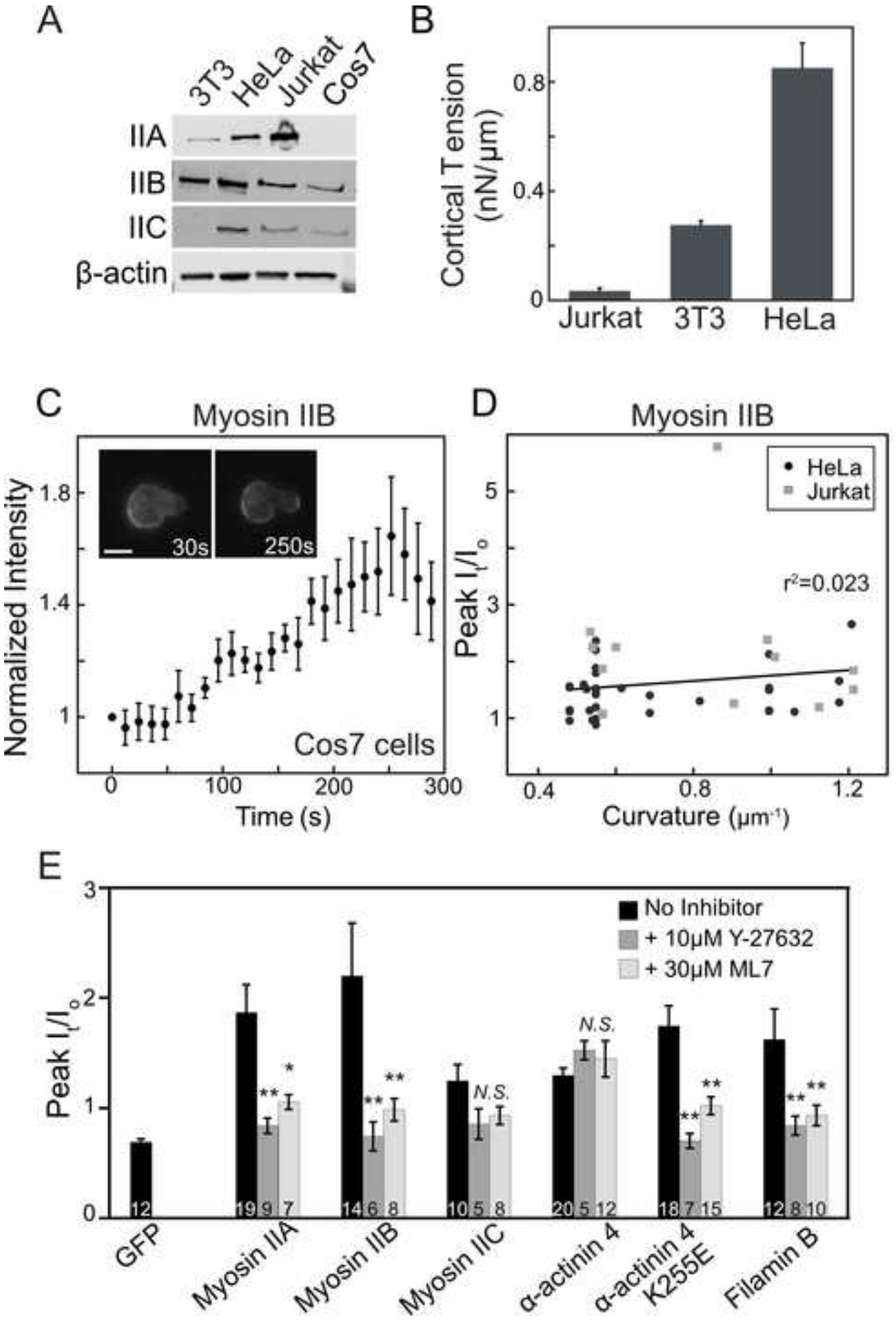

Figure S3

Click here to download Figure SchiffhauerS3.tif

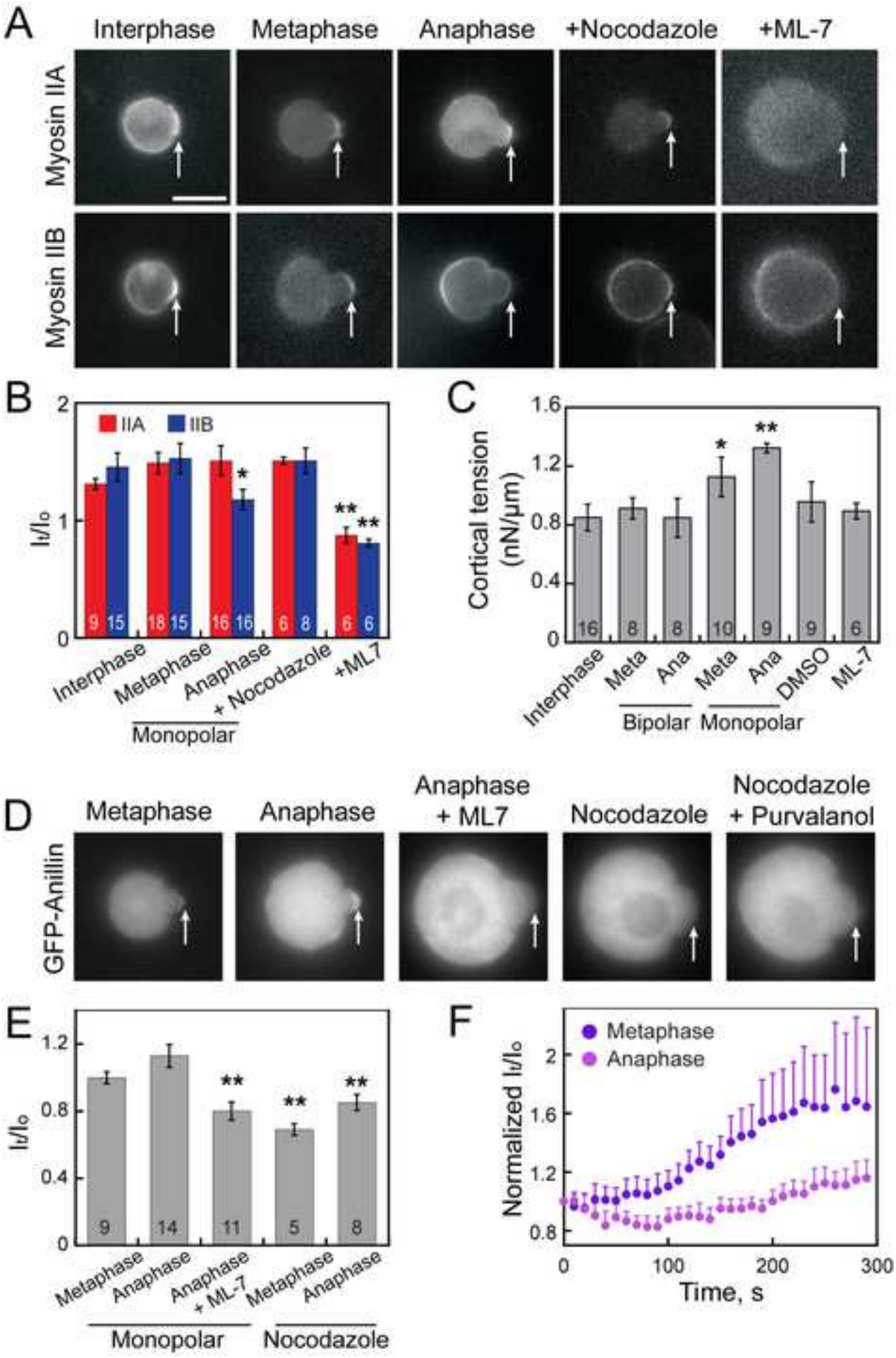

Figure S4

Click here to download Figure SchiffhauerS4.tif

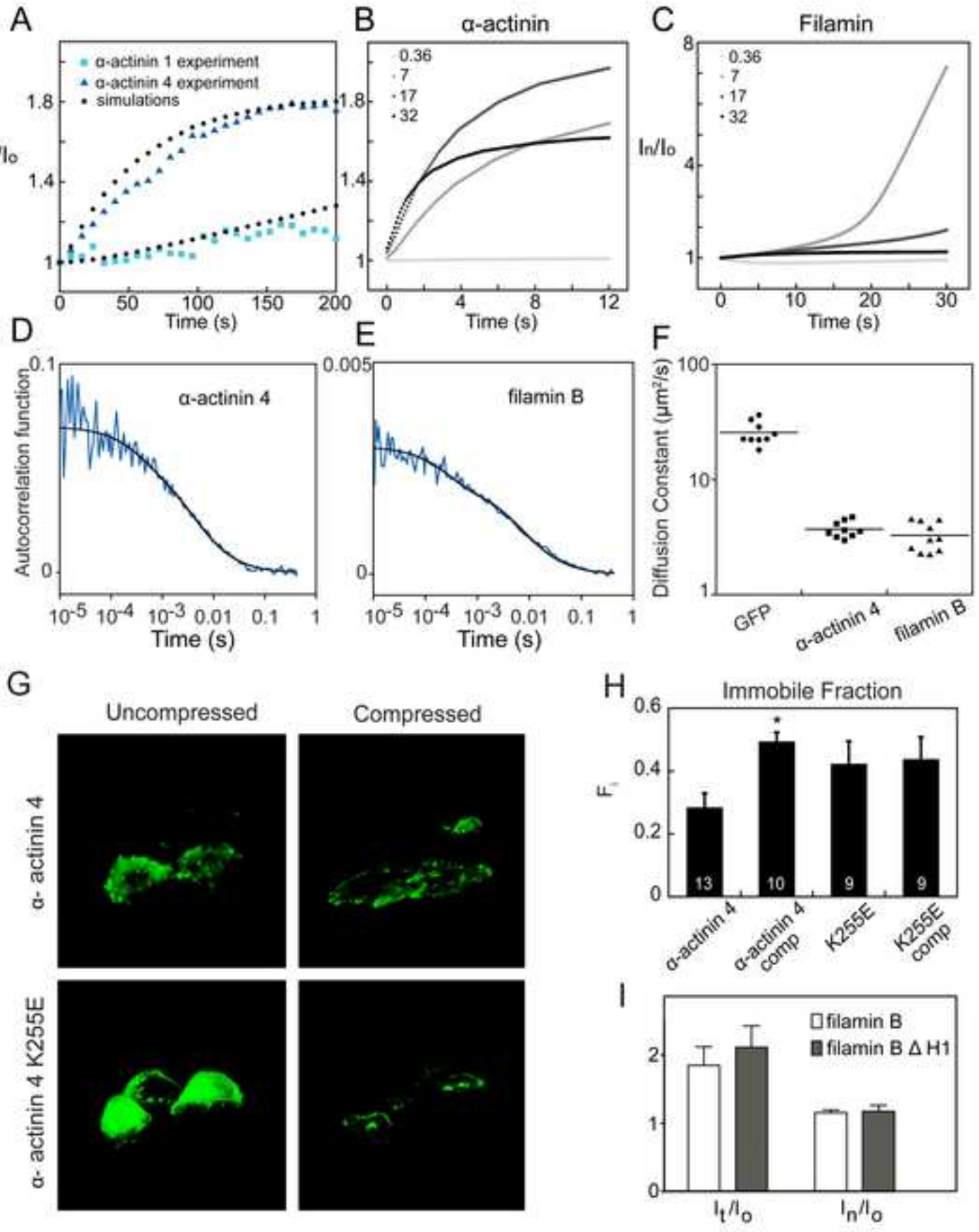

Supplemental Information

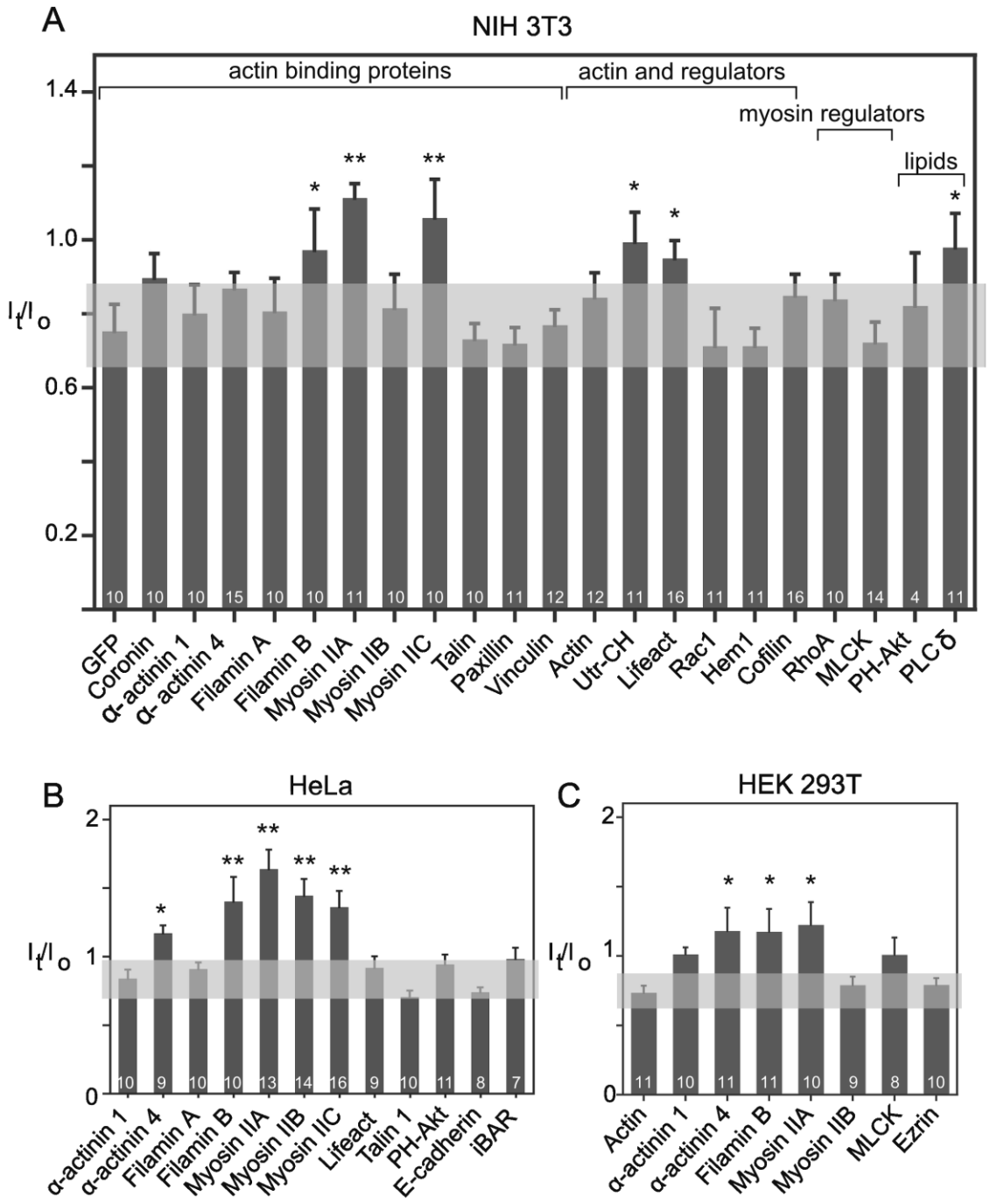

Figure S1

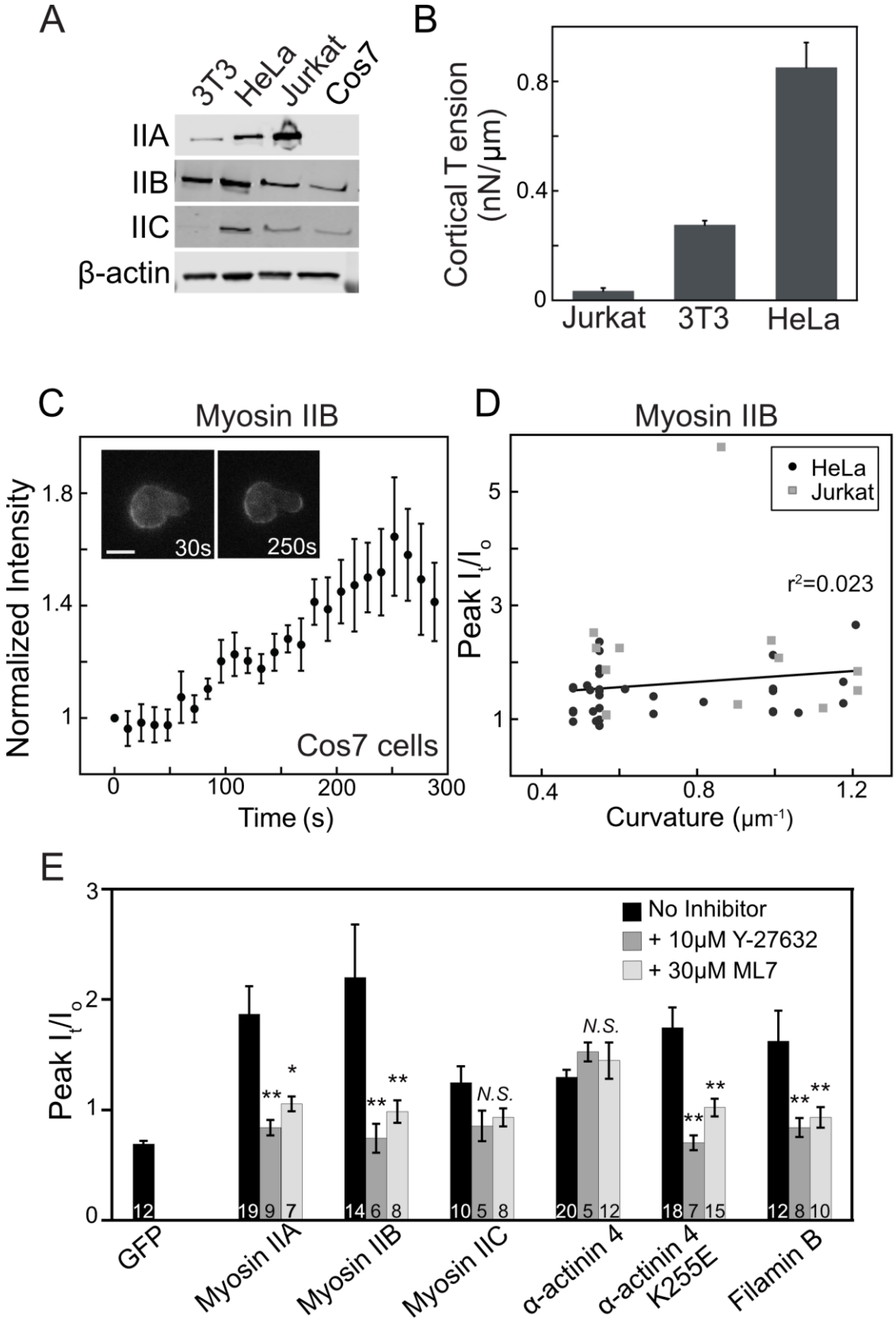
A
3T3
HeLa
Jurkat
Cos7
IIA
IIB
IIC
β-actin
B
Cortical Tension (nN/μm)
0.8
0.4
0
Jurkat
3T3
HeLa
C
Myosin IIB
Normalized Intensity
1.8
1.4
1
30s
250s
Cos7 cells
0
100
200
300
Time (s)
D
Myosin IIB
HeLa
Jurkat
r²=0.023
Peak I_t/I_o
5
3
1
0.4
0.8
1.2
Curvature (μm⁻¹)
E
No Inhibitor
+ 10μM Y-27632
+ 30μM ML7
Peak I_t/I_o
3
2
1
0
N.S.
N.S.
12
19 9 7
14 6 8
10 5 8
20 5 12
18 7 15
12 8 10
GFP
Myosin IIA
Myosin IIB
Myosin IIC
α-actinin 4
α-actinin 4 K255E
Filamin B

Figure S2

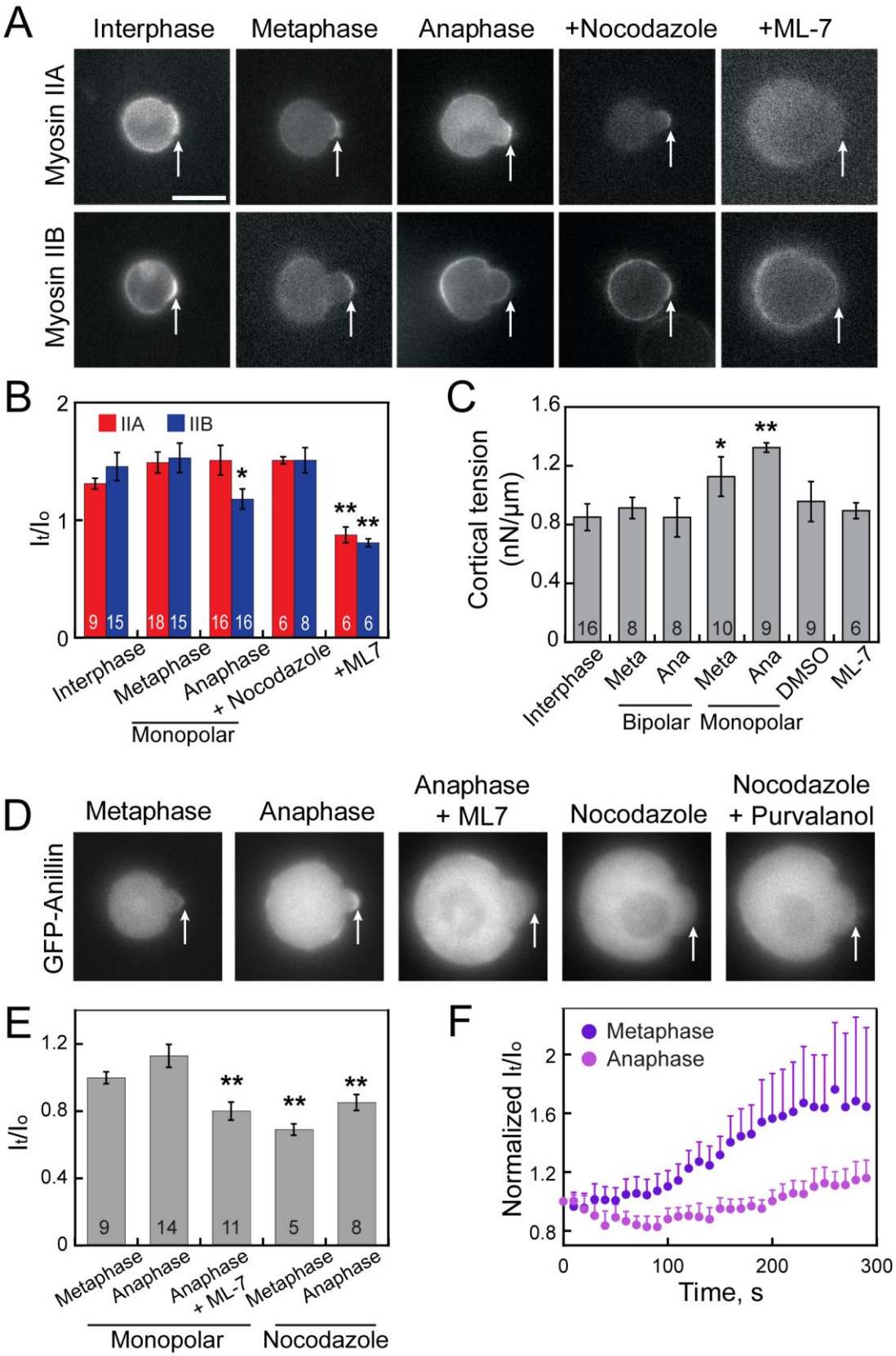
A
Interphase
Metaphase
Anaphase
+Nocodazole
+ML-7
Myosin IIA
Myosin IIB
B
IIA
IIB
It/Io
Interphase
Metaphase
Anaphase
+ Nocodazole
+ML7
Monopolar
C
Cortical tension (nN/μm)
Interphase
Meta
Ana
Meta
Ana
DMSO
ML-7
Bipolar
Monopolar
D
Metaphase
Anaphase
Anaphase + ML7
Nocodazole
Nocodazole + Purvalanol
GFP-Anillin
E
It/Io
Metaphase
Anaphase
Anaphase + ML-7
Metaphase
Anaphase
Monopolar
Nocodazole
F
Metaphase
Anaphase
Normalized It/Io
Time, s

Figure S3

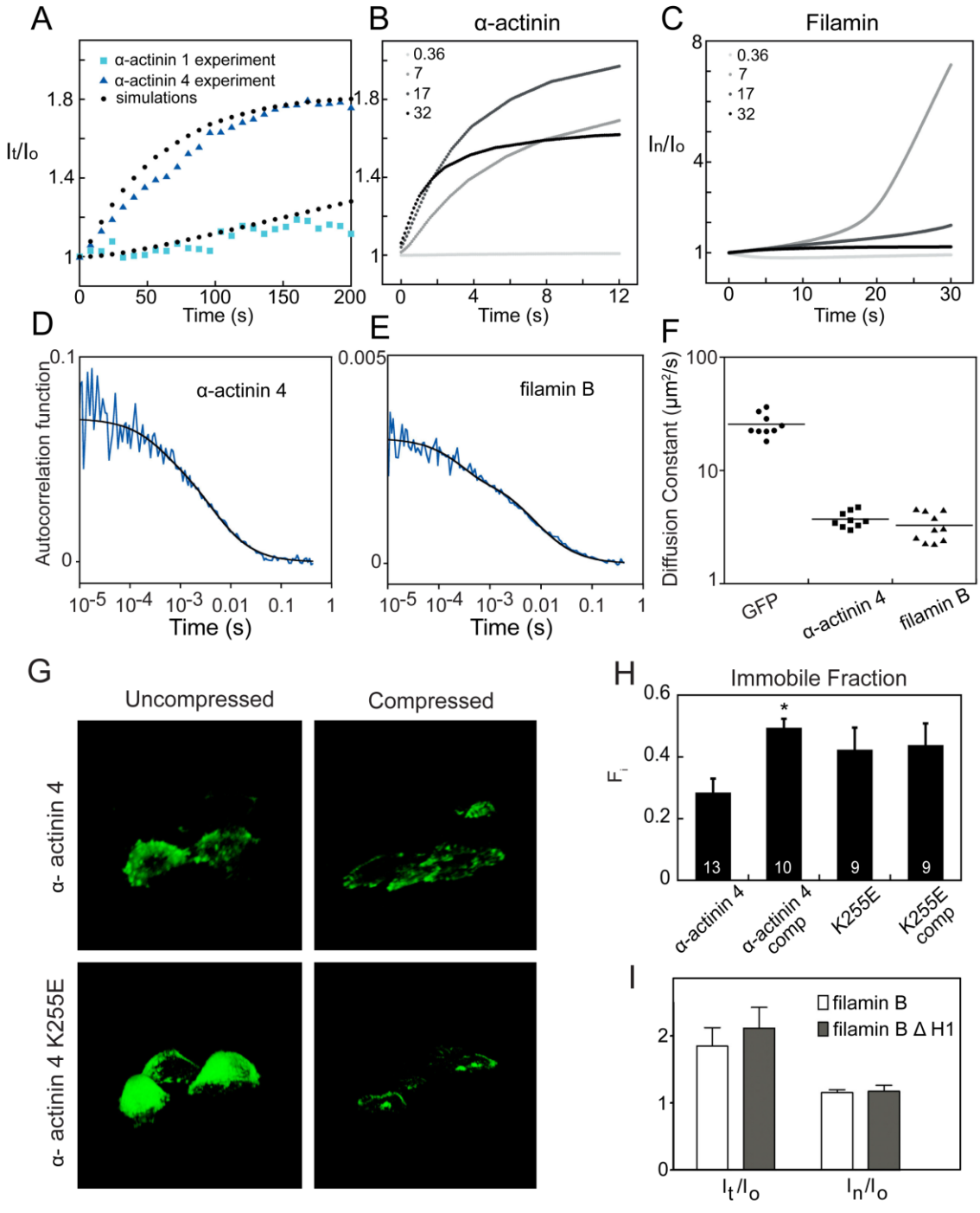
A
α-actinin 1 experiment
α-actinin 4 experiment
simulations
It/Io
Time (s)
B
α-actinin
0.36
7
17
32
Time (s)
C
Filamin
0.36
7
17
32
In/Io
Time (s)
D
α-actinin 4
Autocorrelation function
Time (s)
E
filamin B
Time (s)
F
Diffusion Constant (μm²/s)
GFP
α-actinin 4
filamin B
G
Uncompressed
Compressed
α- actinin 4
α- actinin 4 K255E
H
Immobile Fraction
Fi
13
10
9
9
α-actinin 4
α-actinin 4 comp
K255E
K255E comp
I
filamin B
filamin B Δ H1
It/Io
In/Io

Figure S4

Figure Legends

Figure S1. Actin-binding proteins respond most-strongly to externally-applied mechanical stress. (**A**) In NIH 3T3 cells, (**B**) HeLa cells, and (**C**) HEK 293T cells, α-actinin 4, filamin B, and myosins IIA and IIC showed the most robust accumulation. The peak accumulation of myosin IIB varied between cell types (n values noted on bars, *p<0.05, **p<0.005). The same trends hold for Jurkat cells (**Fig. 1**).

Figure S2. Myosin IIB mechanoresponse is not dependent on endogenous expression or myosin IIA mechanoresponse. (**A**) The actin network as labeled by Lifeact shows a transient initial decrease in fluorescence in HeLa cells due to network dilation (**B**) Neither the endogenous expression of the three myosin II paralogs, nor the resting cortical tension of Jurkat, NIH 3T3, and HeLa cells correlate with myosin IIB mechanoresponse (**Fig. 2B**). Because Cos-7 cells do not express myosin IIA (**A**), yet show robust myosin IIB accumulation to the tip (n=7) (**C**), myosin IIA expression is not required for the myosin IIB mechanoresponse. (**D**) The curvature of the cortex at the tip of cells was estimated as 2/r, where r is the radius of the pipette used for MPA. Curvature was then plotted against the peak accumulation of myosin IIB (I_t/I_o), demonstrating no correlation between curvature and myosin IIB accumulation at the tip. (**Fig. 2B**). (**E**) ML7 and Y-27632 treatments inhibit the peak tip accumulation (normalized to the intensity at the opposite side of the cell (I_t/I_o)) of myosin IIA, myosin IIB, α-actinin 4 K255E, and Filamin B, but not wild-type α-actinin 4, in Jurkat cells (*p<0.005, **p<0.0001 for inhibitor values compared to "No Inhibitor" values). While myosin IIC accumulated significantly in the absence of inhibitor compared with GFP (p<0.05, see Fig. 1), it did not accumulate significantly in the presence of ML7 (p=0.40) or Y-27632 (p=0.62).

Figure S3. Mechanoresponsiveness of myosin II and anillin in HeLa cells. (**A**) Representative micrographs of micropipette aspiration on HeLa cells transiently expressing GFP-myosin IIA or IIB. Nocodazole treatment induces metaphase arrest so these cells are also in metaphase. (Scale bar = 10 μm). (**B**) Average ratio of GFP-myosin II mean intensity at the tip to that at the opposite cortex for aspirated HeLa cells. (**C**) Cortical tension measurements using micropipette aspiration for interphase and mitotic HeLa cells. DMSO and ML7 measurements were performed on interphase cells. (**D**) Representative micrographs of micropipette aspiration on HeLa cells stably expressing GFP-anillin. (**E**) Average ratio of GFP-anillin mean intensity at the tip to that at the opposite cortex. (**F**) Kinetic traces for anillin's mechanosensitive accumulation (normalized to t = 0 s) in monopolar mitotic cells. n value is listed on bars; n for each kinetic trace is the same as listed on corresponding bar in (**E**) (*p < 0.05, **p < 0.005).

Figure S4. Modeling and measuring the mechanisms of filamin and α-actinin mechanoresponse. (**A**) The simulations for α-actinin 1 and α-actinin 4 match the experimentally observed accumulation curve when the on and off rates are slowed by a factor of 8, preserving each protein's K_d. (see **Fig. 3B**). (**B**) For both α-actinin and (**C**) filamin, a catch-bond model predicts poor accumulation at very high binding affinities (K_d = 0.36μM), presumably due to a lack of free monomer in the cytoplasm. (**B**) The K_d of α-actinin 4 (32μM) predicts robust accumulation in the non-cooperative α-actinin model, (**C**) but poor accumulation in the cooperative filamin model. The K_d of filamin B and α-actinin 4 K255E (7μM) predicts accumulation in both models. (**C**) The K_d of filamin A (17μM) predicts no accumulation in the filamin model. Thus, both very high and very low K_d values can inhibit filamin's mechanoaccumulation; the K_d at which the most robust accumulation occurs depends on whether the model is non-cooperative (α-actinin, **Fig. 3B**) or cooperative (filamin, **Fig. 4B**) (**D**) Representative correlation curve measured by FCS for α-actinin 4 in Jurkat cells and (**E**) filamin B in HeLa cells. (**F**) Measured diffusion constants for GFP (26±2.0), α-actinin 4 (3.7±0.20), and filamin B (3.3±0.30). (**G**) Rotated view of a 3D projection of Hela cells, which are flattened to an approximate height of 2 μm when compressed with a sheet of 1% agarose 0.2 mm thick for **Fig. 3E-G.** (**H**) Compressed α-actinin 4 showed a higher immobile fraction (*p=0.007), while there was no significant difference between the immobile fraction of the K255E mutant with and without compression (n values noted on bars). (**I**) A mutant lacking the hinge region of filamin

B did not show a difference in accumulation to the tip (I_t/I_o) or the neck (I_n/I_o) of the aspirated Jurkat cell (n=9).

Table S1. Parameters for α-actinin modeling.

Parameter	Value	Reference
$[F_1]$	72 μM	[S16]
$[F_2]$	8 μM	[13]
D_1 (ACTN)	3.7 $\mu m^2 s^{-1}$	Measured
$D_{2,3}$ (cortex)	$D_1/50$	Calculated using parameters outlined in [13]
$D_{2,3}$ (cytoplasm)	D_1	Calculated using parameters outlined in [13]
K_D	0.36 μM (ACTN1), 7 μM, 17 μM, or 32 μM (ACTN4)	[S17] [S18] [S19] [30]
$k_{on\ 1,2}^0$	1.1 $\mu M^{-1}\ s^{-1}$	[S20]
$k_{off\ 1,2}^0$	0.4 s^{-1} (ACTN1), 7.7 s^{-1}, 19 s^{-1}, or 35 s^{-1} (ACTN4)	[S17] Calculated from K_D Calculated from K_D Calculated from K_D

Table S2. Parameters used in filamin model simulations.

Parameter	Value	Reference
$[F_1]$	100 μM	[25]
$[F_2]$	5 μM	[13]
D_1 (filamin)	3.3 $\mu m^2 s^{-1}$	Measured
D_2 (cortex)	0.03 $\mu m^2 s^{-1}$	[13]
D_3 (cortex)	0.003 $\mu m^2 s^{-1}$	[13]
$D_{2,3}$ (cytoplasm)	D_1	
K_D	0.36 μM, 7 μM (FLNA), 17 μM (FLNB), or 32 μM	[S17] [S18] [S19] [30]
$k_{on\,1}{}^0$	1.3 $\mu M^{-1}\ s^{-1}$	[S21]
$k_{on\,2}{}^0$	0.013 $\mu M^{-1}\ s^{-1}$	Estimated from sensitivity analysis, [13]
$k_{off\,1}{}^0$	0.47 s^{-1}, 9.1 s^{-1} (FLNB), 22 s^{-1} (FLNA), or 41 s^{-1}	Calculated from K_D Calculated from K_D Calculated from K_D Calculated from K_D
$k_{off\,2}{}^0$	0.047 s^{-1}, 0.91 s^{-1} (FLNB), 2.21 s^{-1} (FLNA), or 4.1 s^{-1}	Estimated from sensitivity analysis[1], [13] Estimated from sensitivity analysis[1], [13]
Δx^{α} Δx^{β}	0.194 nm -0.194 nm	[S17] [S17]
χ	8	[13], sensitivity analysis[1]

[1]Extensive sensitivity analysis was performed based on parameters described in [13] with little difference in the result with values above or below.

Supplemental Materials and Procedures

Cell culture

Jurkat cells were cultured in RPMI 1640 (Sigma-Aldrich) with 10% FBS (Life Technology). HeLa, Cos-7, and NIH 3T3 cells were cultured in DMEM (Life Technology) with 10% FBS. For MPA experiments, adherent cells were cultured on tissue-culture treated dishes (Corning), detached using 0.5% trypsin (Life Technology), centrifuged and resuspended in media. Cortical tension was calculated as described previously [12]. Transient transfections were performed using FuGene HD (Promega) for adherent cells, and electroporation for Jurkat cells. For FRAP studies, HeLa cells were cultured on glass-bottom dishes (Corning) and transferred to Leibowitz Media (Life Technology) + 10% FBS four hours prior to imaging.

Constructs

The following plasmids were acquired from Addgene:

Construct	Addgene Number	Resource
EGFP-C1-β-actin	31949	Vladislav Verkhush [S1]
Mcherry-UtrCH-pCS2	26740	William Bement [S2]
mCherry-Ezrin-C14	55042	Michael Davidson
EGFP-C1-Talin	26724	Anna Huttenlocher [S3]
EFGP-N1-ACTN1	11908	Carol Otey [S4]
Mcherry-N1-coronin1B	27694	Christien Merrifield [S5]
E-cadherin-GFP	28009	Jennifer Stow [S6]
EGFP-C1-PH-PLCδ	21179	Tobias Meyer [S7]
mCherry-C1-cofilin	27687	Christien Merrifield [S5]
EGFP-MLCK-C2	46316	Anne Bresnick [S8]

The Ras-binding domain sequence from human Raf and the PH domain of human AKT were cloned into the FUW2 vector, tagged with GFP and mCherry respectively. GFP tagged constructs for EGFP-C3-myoIIA [S9], EGFP-C3-myoIIB [S9], and EGFP-N3-myoIIC [S10], were gifts from Robert Adelstein. CFP-C1-Kras, EYFP-C1-Rac1, mCherry-iBAR, and Lifeact-RFP-N1 were gifts from Allison Suarez and Takanari Inoue. EGFP-N1-ACTN4 was a gift from Allan Wells [S11]. A point mutation K255E was made in EGFP-N1-ACTN4 by site-directed mutagenesis to generate EGFP-N1-ACTN4 (K255E). The filamin A construct, pmdsRed-FLNA, was a gift from Fumihiko Nakamura. Filamin B full length construct EGFP-FLNB-pCI-C1, and hinge 1 deletion mutant construct EGFP-FLNB(ΔH1)-pCI-C1 were gifts from Arnoud Sonnenberg [S12]. Constructs for Septin 1 and 7, EGFP-N1-sept1 and EGFP-C1-sept7, were gifts from William Trimble [S13]. EYFP-paxillin and EGFP-vinculin were gifts from Susan Craig [S14]. GFP-anillin was stably expressed from a BAC and was a gift from Anthony Hyman [S15].

Drug treatment

Myosin II light chain inhibitor ML7 (Sigma I2764) was dissolved in DMSO. The final concentration of DMSO in culture medium was kept below 0.15% during drug treatment. After resuspension, cells were treated with DMSO or ML7 for 15 minutes prior to imaging. ROCK inhibitor Y-27632 was dissolved in water, and cells were treated 30 minutes prior to imaging. For making measurements in mitotically arrested cells, 20 μM STLC was added for 4 hours. Anaphase onset was induced by adding 30 μM purvalanol A, followed by 15-30 minutes incubation. Microtubule depolymerisation was carried out by treating with 1 μg/mL nocodazole for 4 hours.

Measurements of mechanosensory response of proteins using micropipette aspiration
Micropipette aspiration was performed as described previously [12]. In short, a pressure difference was generated by adjusting the height of a motor-driven water manometer. Mammalian cells expressing desired fluorescent proteins were loaded into the observation chamber, which was filled with either DMEM or RPMI 1640 medium depending on the cell type. Cell types were deformed equally using the ratio of the aspirated length of the cell in the pipette (L_p) over the radius of the pipette (R_p) as a guide. Once a pressure was determined for each cell type for which L_p/R_p was approximately equal to two, this fixed pressure was used for all cells of that type. These values were different between cell types (0.075 nN/μm^2 for Jurkat cells, 0.15 nN/μm^2 for NIH 3T3 cells, 0.2 nN/μm^2 for HeLa cells, and 0.15nN/ μm^2 for Cos-7 cells) due to the unique cortical tensions of these cells (**Fig. S2B**). Pressures higher than this often led to blebbing, or the separation of cell membrane from the cortex. All cells which demonstrated blebbing at any time during recording were discarded. Images were collected with an Olympus IX81 microscope equipped with MetaMorph software and analyzed using ImageJ (National Institutes of Health). After background correction, the fluorescence intensity at the accumulation sites inside the micropipette were normalized against the opposite cortex of the cell. This was repeated for each frame to obtain time-courses and account for expression level variation and photobleaching.

Measurement of fluorescence recovery after photobleaching (FRAP)
FRAP was performed as described previously [15]. HeLa cells were plated at low density on glass-bottom dishes and transiently transfected 40 hours prior to imaging. The culture media was changed to Leibowitz Media four hours prior to imaging. FRAP experiments were performed using a Zeiss AxioObserver with 780-Quasar confocal module, with a 63x (NA 1.4) objective at 37C and 5% CO_2. A small region of the cell cortex was bleached using a 488 nm Argon laser, and the fluorescence recovery was recorded until recovery saturated (100 frames, 5-15 s/frame depending on the protein). The size and placement of the bleach region was kept relatively constant across measurements. For each frame, the average intensity of the bleached cortical region, reference (unbleached) region, and background was quantified using ImageJ (National Institutes of Health). For photobleaching correction, the reference theoretical intensity (RTI) was calculated by fitting the background subtracted reference intensity to an exponential decay equation as follows:

(1) $$RTI(t) = A - B \cdot e^{-Ct}$$

where A, B and C are fitting parameters.

The intensity of the bleached region was background subtracted and normalized to RTI. The normalized intensity (NI) was obtained by normalizing this to the pre-bleach intensity (average of 4 pre-bleach images), and was fitted to a single exponential as follows:

(2) $$NI(t) = m_1(1 - m_2 \cdot e^{-kt})$$

Where m_1, m_2 are fitting parameters and k is the recovery rate.
The recovery time, τ, and the immobile fraction, F_i were measured as:

(3) Recovery time, $\tau = 1/k$

(4) Immobile fraction, $F_i = \frac{1-m_1}{1-m_1+m_2}$

Measurement of diffusion time by fluorescence correlation spectroscopy (FCS)
Jurkat (ACTN4) or HeLa (FLNB) cells were plated at low confluence in glass bottom dishes, transiently transfected 40 hours prior to imaging, and media was replaced with Leibowitz media 4 hours prior to imaging. FCS was performed exactly as previously described [15] at 37C and 5% CO_2 on a Zeiss AxioObserver with 780-Quasar confocal module & FCS, with a C-Apochromat 40x (NA 1.2) water objective.

Modeling the catch-bond behavior of α-actinin and filamin
A full explanation of the molecular model used to predict the behavior of α-actinin and filamin in *Dictyostelium* is published [13]. In short, α-actinin is a dimer containing two actin-binding domains (ABD). One ABD of the protein first binds a single actin filament, where its diffusivity becomes greatly reduced, and it searches for a second filament to bind within a 3D sphere with a radius equal to the length of the protein rod. This binding reaction can be written as $[Cr]+[F_1]\leftrightarrow[CrF_1]+[F_2]\leftrightarrow[CrF_1F_2]$ where *Cr*, F_1, and F_2 correspond to the crosslinker, the actin filament in the first step, and the actin filament in the second step, respectively. The reaction-diffusion equations used to model these conditions are as follows:

$$\frac{\partial[Cr]}{\partial t} = D_1\nabla^2[Cr] - (k_{\text{on1}}[Cr][F_1] - k_{\text{off1}}[CrF_1])$$

$$\frac{\partial[CrF_1]}{\partial t} = D_2\nabla^2[CrF_1] + (k_{\text{on1}}[Cr][F_1] - k_{\text{off1}}[CrF_1]) - (k_{\text{on2}}[CrF_1][F_2] - k_{\text{off2}}[CrF_1F_2]) \quad (5)$$

$$\frac{\partial[CrF_1F_2]}{\partial t} = D_3\nabla^2[CrF_1F_2] + (k_{\text{on2}}[CrF_1][F_2] - k_{\text{off2}}[CrF_1F_2])$$

where D_1, D_2, and D_3 are the diffusion constants of Cr , CrF_1, and CrF_1F_2, and k_{on1}, k_{on2}, k_{off1}, and k_{off2} are the on and off rates for the first and second steps, respectively. To simulate catch-bond behavior, we assumed the force-dependent binding condition would be the one in which the crosslinker is bound to two filaments. We used the following equation to make the second off rate slow with the application of force:

$$k_{\text{off2}} = k^0_{\text{off2}}\exp(-f\Delta x/k_{\text{B}}T) \quad (6)$$

where k^0_{off2} is the zero-force off rate, f is the force applied, and Δx is the phenomenological bond length in a Bell-type model [S22].

Filamin also forms dimers and undergoes a two-step binding reaction with actin, however it binds orthogonal filaments which may not be at right angles, and different filament angles lead to different off rates for filamin [S17]. Thus, we use α to denote angles less than 90°, and β to denote angles greater than 90° in the following reaction-diffusion equations for filamin:

$$\frac{\partial[Cr]}{\partial t} = D_1\nabla^2[Cr] - (k_{\text{on1}}[Cr][F_1] - k_{\text{off1}}[CrF_1])$$

$$\frac{\partial[CrF_1]}{\partial t} = D_2\nabla^2[CrF_1] + (k_{\text{on1}}[Cr][F_1] - k_{\text{off1}}[CrF_1]) - (k_{\text{on2}}[CrF_1] - k^{\alpha}_{\text{off2}}[Cr^{\alpha}F_1F_2]) - \left(k_{\text{on2}}[CrF_1][F_2] - k^{\beta}_{\text{off2}}[Cr^{\beta}F_1F_2]\right) \quad (7)$$

$$\frac{\partial[Cr^{\alpha}F_1F_2]}{\partial t} = D_3\nabla^2[Cr^{\alpha}F_1F_2] + (k_{\text{on2}}[CrF_1][F_2] - k^{\alpha}_{\text{off2}}[Cr^{\alpha}F_1F_2])$$

$$\frac{\partial[Cr^{\beta}F_1F_2]}{\partial t} = D_3\nabla^2[Cr^{\beta}F_1F_2] + \left(k_{\text{on2}}[CrF_1][F_2] - k_{\text{off2}}^{\beta}[Cr^{\beta}F_1F_2]\right)$$

In the case of filamin, we used **Equation 6** to incorporate catch-bond behavior into k_{off2}, but also incorporated structural cooperativity into k_{on2} using the following equation:

(8) $$k_{\text{on2}} = k_{\text{on2}}^{0}\left(1 + \frac{[Cr^{\alpha}F_1F_2]+[Cr^{\beta}F_1F_2]}{F_2}\right)^{x\cos\theta}$$

where x is the cooperativity index and θ is the azimuth angle in the tip of an aspirated cell. See **Table S1** and **Table S2** for the parameters used for each variable.

Statistical analysis

Statistical analysis was performed using Graph Prism (www.graphpad.com) or KaleidaGraph (Synergy Software). The Mann-Whitney test was used for non-parametric comparisons of different data sets. Data sets were also analyzed by analysis of variance (ANOVA) with a Fisher's least significant difference comparison. Both methods obtained nearly identical conclusions.

Supplemental References

S1. Subach, F.V. *et al.* (2009). Photoactivatable mCherry for high-resolution two-color fluorescence microscopy. Nat. Methods. *6*, 153-159.

S2. Burkel, B.M., von Dassow, G., and Bement, W.M. (2007). Versatile fluorescent probes for actin filaments based on the actin-binding domain of utrophin. *Cell Motil.* Cytoskeleton. *64*, 822-832.

S3. Franco, S.J. *et al.* (2004). Calpain-mediated proteolysis of talin regulates adhesion dynamics. Nat. Cell Biol. *6*, 977-983.

S4. Edlund, M., Lotano, M.A., and Otey, C.A. (2001). Dynamics of alpha-actinin in focal adhesions and stress fibers visualized with alpha-actinin green fluorescent protein. Cell Motil. Cytoskeleton. *48*, 190-200.

S5. Taylor, M.J., Perrais, D., and Merrifield, C.J. (2011). A high precision survey of the molecular dynamics of mammalian clathrin-mediated endocytosis. PLoS Biol. *9*, e1000604.

S6. Miranda, K.C. *et al.* (2001). A dileucine motif targets e-cadherin to the basolateral cell surface in Madin-Darby canine kidney and LLC-PK1 epithelial cells. J. Biol. Chem. *276*, 22565-22572.

S7. Stauffer, T.P., Ahn, S., and Meyer, T. (1998). Receptor-induced transient reduction in plasma membrane PtdIns(4,5)P2 concentration monitored in living cells. Curr. Biol. *8*, 343-346.

S8. Dulyaninova, N.G., Patovsky, Y.V., and Bresnick, A.R. (2004). The N-terminus of the long MLCK induces a disruption in normal spindle morphology and metaphase arrest. J. Cell Sci. *117*, 1481-1493

S9. Wei, Q., and Adelstein, R.S. (2000). Conditional expression of a truncated fragment of nonmuscle myosin II-A alters cell shape but not cytokinesis in HeLa cells. Mol. Biol. Cell **11**, 3617-3627

S10. Golomb, E., *et al.* (2004). Identification and characterization of nonmuscle myosin II-C, a new member of the myosin II family. J. Biol. Chem *279*, 2800-2808.

S11. Shao, H., Wang, J. H., Pollak, M.R., and Wells, A. (2010). α-Actinin-4 is essential for maintaining the spreading, motility and contractility of fibroblasts. PloS one. *5*, e13921.

S12. van der Flier, A. *et al*. (2002). Different splice variants of filamin-B affect myogenesis, subcellular distribution, and determine binding to integrin β subunits. J. Cell Biol. *156*, 361-376.

S13. Huang, Y.W. *et al*., (2008). Mammalian septins are required for phagosome formation. Mol. Biol. Cell**.** *19*, 1717-1726.

S14. Chen, H., Cohen, D. M., Choudhury, D.M., Kioka, N., and Craig, S.W. (2005). Spatial distribution and functional significance of activated vinculin in living cells. J. Cell Biol. *169*, 459-470.

S15. Poser, I. *et al*. (2008). BAC TransgeneOmics: a high-throughput method for exploration of protein function in mammals. Nat. Methods *5*, 409-415.

S16. Haugwitz, M., Noegel, A.A., Karakesisoglou J., and Schleicher, M. (1994). *Dictyostelium* amoebae that lack G-actin-sequestering profilins show defects in F-actin content, cytokinesis, and development. Cell. *79*, 303-314.

S17. Ferrer, J.M. *et al.* (2008). Measuring molecular rupture forces between single actin filaments and actin-binding proteins. Proc. Natl. Acad. Sci. U S A. *105*, 9221-9226.

S18. Sawyer, G.M., Clark, A.R., Robertson, S.P., and Sutherland-Smith, A.J. (2009). Disease-associated substitutions in the filamin B actin binding domain confer enhanced actin binding affinity in the absence of major structural disturbance: Insights from the crystal structures of filamin B actin binding domains. J. Mol. Biol. *390*, 1030-47.

S19. Nakamura, F., Osborn, T.M., Hartemink, C.A., Hartwig, J.H., and Stossel, T.P. (2007). Structural basis of filamin A functions. J. Cell Biol. *179*, 1011-1025.

S20. Wachsstock, D.H., Schwarz, W.H., and Pollard, T.D. (1994).Cross-linker dynamics determine the mechanical properties of actin gels. Biophys J. *66*, 801-809

S21. Goldmann, W.H., and Isenberg, G. (1993). Analysis of filamin and alpha-actinin binding to actin by the stopped flow method. FEBS Lett. *336*, 408-410.

S22. Bell, G.I. (1978). Models for the specific adhesion of cells to cells. Science *200*, 618-627.